A 3D BIOPRINTED IN VITRO MODEL OF HUMAN LIVER FOR THE STUDY OF LIVER FIBROSIS

A Dissertation
Presented to
The Academic Faculty

by

Linqi Jin

In Partial Fulfillment
of the Requirements for the Degree
Master of Science in the
Wallace H. Coulter Department of Biomedical Engineering

Georgia Institute of Technology and Emory University
August 2021

A 3D BIOPRINTED IN VITRO MODEL OF HUMAN LIVER FOR THE STUDY OF LIVER FIBROSIS

Approved by:

Dr. Vahid Serpooshan, Advisor
Department of Biomedical Engineering
Georgia Institute of Technology & Emory University

Dr. Holly Bauser-Heaton
School of Medicine
Emory University

Dr. Scott J. Hollister
Department of Biomedical Engineering
Georgia Institute of Technology & Emory University

Dr. Sung-Jin Park
Department of Biomedical Engineering
Georgia Institute of Technology & Emory University

Date Approved: May 14, 2021

ACKNOWLEDGEMENTS

Foremost, I would like to express my sincere thanks to my thesis advisor, Dr. Vahid Serpooshan for his patience, trust, continuous encouragement, and perceptive guidance throughout my Master's study. The completion of this thesis would not have been possible without his help and support. Thanks for providing me insightful feedbacks and inspiring ideas to formulate the research methodology of this work and setting up such an incredible example of work ethics. It is a great honor to be your student and get the privilege to spend these special two years focusing on this project. The invaluable experience shaped me into a better self.

Much appreciation to my lab members. Thank you all so much for creating a pleasant environment to work in the lab, looking after my cell cultures, and having thought-provoking discussions with me. I would like to acknowledge Dr. Holly Bauser-Heaton for offering constructive comments, Dr. Martin Tomov for helping address technical issues, Dr. Liqun Ning, Boeun Hwang, Andrea Theus, and Lilanni Perez for answering all my questions and keeping me great company, Shuai Chen, Carmen Gil, Melissa Cadena, and Keno Ogelohwohor for being motivating fellows. Special thanks to Dr. Archana Kamalakar for helping me with assays and Dr. Jinqi Fan for driving me home late at night.

I would also like to acknowledge my close friends who allowed me to always be genuine and bold, and kept my life joyful even at difficult times.

Finally, I would like to thank my dear parents for their unconditional love, understanding, and support.

TABLE OF CONTENTS

LIST OF TABLES

LIST OF FIGURES

LIST OF SYMBOLS AND ABBREVIATIONS

ECM	Extracellular Matrix
3D	Two-Dimensional
NAFLD	Non-Alcoholic Fatty Liver Disease
NASH	Non-Alcoholic Steatohepatitis
HSC	Hepatic Stellate Cell
2D	Three-Dimensional
EC	Endothelial Cell
GelMA	Gelatin Methacrylate
PBS	Phosphate Buffer Saline
CAD	Computer-Aided Design
UV	Ultraviolet
EMEM	Eagle's Minimum Essential Medium
FBS	Fetal Bovine Serum
EDTA	Ethylenediaminetetraacetic Acid
HUVEC	Human Umbilical Vein Endothelial Cell
GFP	Green Fluorescent Protein
VEGF	Vascular Endothelial Growth Factor
IHC	Immunohistochemical
ELISA	Enzyme-Linked Immunosorbent Assay
BSA	Bovine Serum Albumin
SEM	Standard Error of the Mean
Hep	Hepatocyte

SUMMARY

Liver fibrosis, a characteristic of most liver diseases, results from chronic liver injury in conjunction with the accumulation of extracellular matrix (ECM) proteins[1,2]. Despite the critical role of liver tissue microenvironmental changes in the development and progression of liver fibrosis[3,4], the cellular mechanisms underlying hepatic dysfunction in liver fibrosis in response to mechanical cues (e.g., ECM stiffness and dynamic flow) remain elusive. In this study, we fabricated three-dimensional (3D) perfusable liver models with ECM stiffness values mimicking those in the healthy *vs.* fibrotic states of the human liver. Engineered liver models retained viability, proliferation, and function of both human endothelial and hepatic cells during a 2-week culture period. Further, the effects of hepatocyte-endothelial cell coculture and dynamic flow conditions (static *vs.* rocking) were studied in our 3D bioprinted model of liver fibrosis. Finally, a pilot perfusion study was successfully conducted using a customized bioreactor system, demonstrating the robust potential of this 3D bioprinted liver platform to be utilized for intensive *in vitro* studies of liver diseases.

CHAPTER 1. INTRODUCTION

1.1 Liver Fibrosis

1.1.1 Causes, Pathophysiology and Stages of Liver Fibrosis

Liver diseases have been a leading cause of death worldwide[5,6]. Every year, approximately 2 million deaths are due to liver diseases globally[7,8]. Liver fibrosis, which results from chronic liver injury in conjunction with the accumulation of extracellular matrix (ECM) proteins, is a characteristic of most liver diseases[1,2]. Common causes of liver fibrosis include infection with the hepatitis B and C virus, non-alcoholic fatty liver disease (NAFLD), non-alcoholic steatohepatitis (NASH), cholestatic liver diseases, autoimmune diseases, metabolic disorders, alcohol abuse, and drug toxicity[1,9]. Damaged hepatocytes produce various mediators such as reactive oxygen species and fibrogenic cytokines, which in turn activate hepatic stellate cells (HSC) to differentiate into myofibroblasts, along with promoting HSCs and other fibrogenic cells to produce excessive ECM proteins[10]. The excessive accumulation of connective tissue in the liver leads to the formation of fibrous scars. Subsequently, the distortion of hepatic architecture and development of regenerating hepatocyte nodules progress to liver fibrosis, cirrhosis, which potentially leads to hepatocellular carcinoma and/or liver failure, if not prevented[7,9,11]. Further, the recruitment of immune cells and the activation of Kupffer cells and macrophages in the liver caused by chronic liver injury can promote the progression of liver fibrosis via the secretion of inflammatory and fibrogenic cytokines (**Figure 1**)[12,13]. Following the development of cirrhosis, hepatocellular dysfunction and increased intrahepatic resistance to blood flow will often result in a series of complications including hepatic insufficiency and portal

hypertension[14-16].

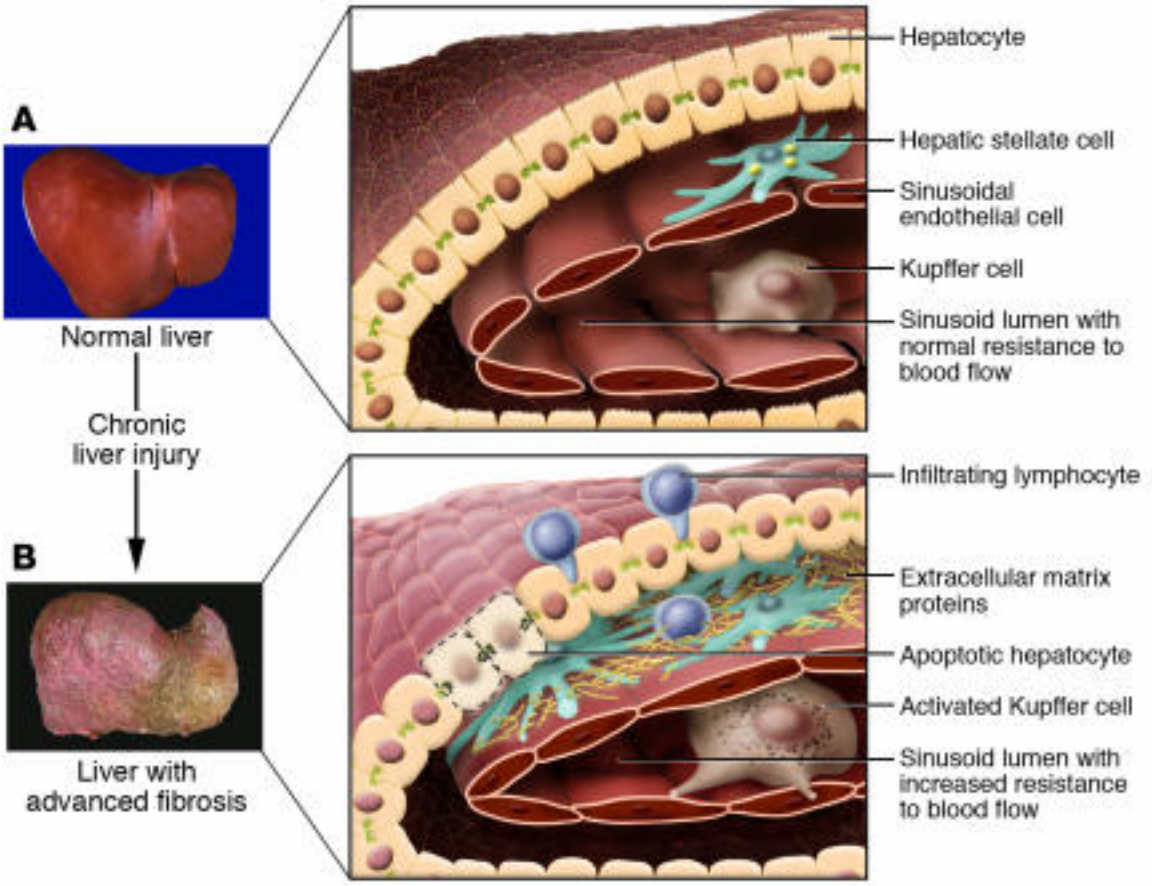

Figure 1. Changes in the hepatic tissue architecture. (**A**) associated with advanced hepatic fibrosis (**B**). Adapted with permission[17]. Copyright © 2005, American Society for Clinical Investigation.

Traditionally, liver biopsy is considered the "gold standard" of examining liver fibrosis[18]. In recent years, the noninvasive imaging test of transient elastography (FibroScan®) has been widely used to measure liver stiffness (i.e., elastic modulus). According to the measured moduli, liver fibrosis is classified into multiple stages (Table 1)[18-21]. It is known that liver tissue microenvironmental changes play a critical role in the development and progression of liver fibrosis via HSC activation[3,4]. However, the cellular

mechanisms underlying hepatic dysfunction in response to mechanical cues (including ECM stiffness and dynamic flows) remain elusive, which has hampered the effective prevention, early diagnostics, and development of therapeutics for liver fibrosis. In this study, we fabricated three-dimensional (3D) perfusable liver models with ECM stiffness values mimicking those at the healthy (F0) *vs.* fibrotic (F4) states of the human liver. We introduced dynamic tissue culture conditions to recapitulate the dynamic liver microenvironment *in vivo* (shear stress, nutrient/oxygen diffusion) and studied the effects of dynamic flows and hepatocyte-HUVEC coculture on hepatic function.

Table 1. Elastic modulus alterations in human liver tissue at different stages of fibrosis.

Fibrosis Stage	F0 to F1	F2	F3	F4
Scarring	no to mild fibrosis	moderate fibrosis	severe fibrosis	cirrhosis
Elastic modulus (kPa)	< 6	6-8	8-12.5	> 12.5

1.1.2 In Vitro and In Vivo Models of Liver Fibrosis

Previous studies have described a variety of animal models[22,23] and *in vitro* liver models[24-26] that mainly comprised of two-dimensional (2D) or suspension cultures of human hepatocytes for liver disease modeling and drug screening applications (**Figure 2**)[27]. Experimental animal models, besides the high cost and ethical issues, face inherent drawbacks of having metabolic and hemodynamic differences from the actual human liver microenvironment[28]. On the other hand, most *in vitro* models used to study liver fibrosis

are focused on HSC genotypic and phenotypic alterations, their regulation of sinusoidal blood flow, and the synthesis and degradation of ECM proteins[29,30]. Several studies have been described to develop coculture models of primary HSC or cell lines with Kupffer cells, endothelial cells (ECs), or hepatocytes, by plating one cell type on culture inserts or coverslips[31-34], or plating a mixture of non-parenchymal cells on top of a hepatocyte-laden collagen gel[35,36]. However, most of these platforms remain within a 2D monolayer scale, facing a rapid loss of function, lack of hepatic sinusoid heterogeneity, and *in vivo*-like cellular interactions. Whereas 3D liver models consisting of spheroids or organoids mainly are limited to static culture conditions, imprecise structural control, and inaccurate repeatability[37-39].

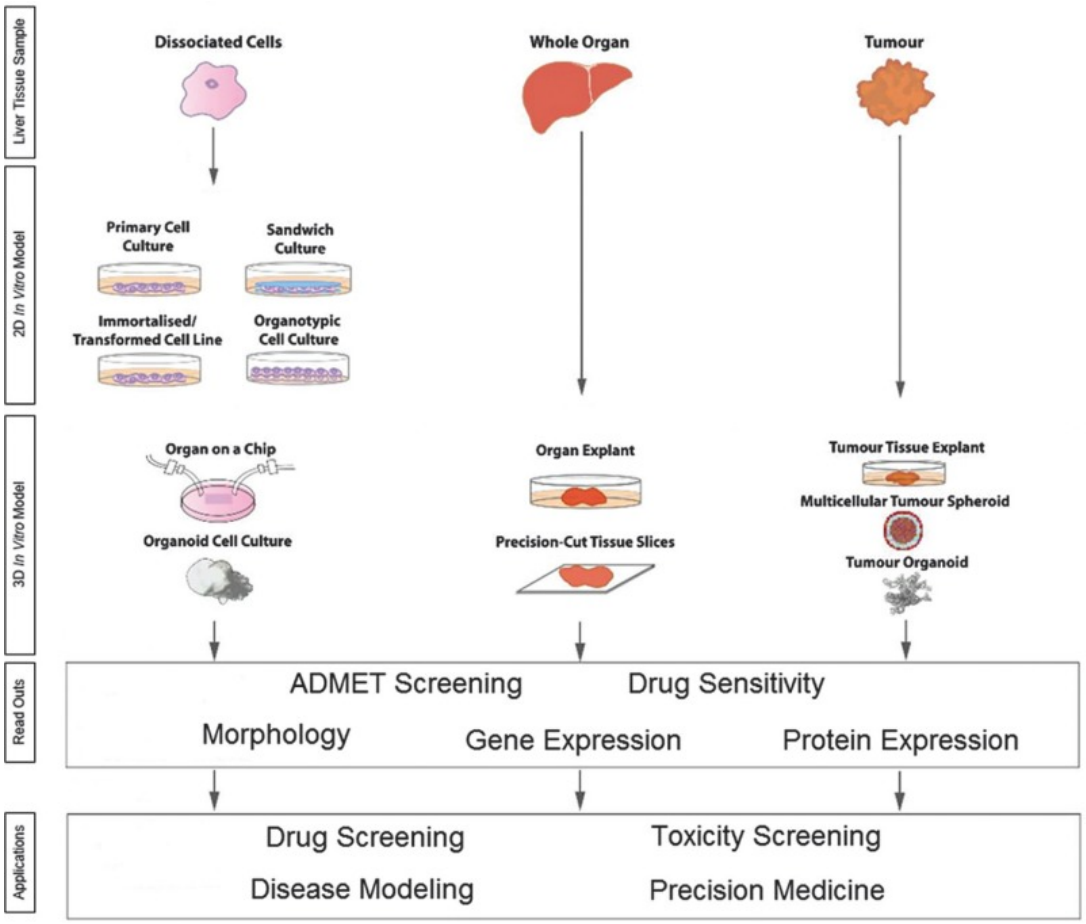

Figure 2. Overview of 2D and 3D *in vitro* models of the liver. Flow diagram indicates the *in vitro* models of the liver, their readouts, and applications. Each model was categorized by the type of sample it is derived from and whether it is 2D or 3D model. Adapted with permission[37].

Suboptimal *in vitro* liver models have hindered the advancement of translational research in the fields of liver tissue engineering and regenerative medicine[5,40]. The newly emerging advanced biomanufacturing technologies, and in particular, 3D bioprinting methods, have shown great promise as an alternative technique to create functional liver tissue analogues. 3D bioprinting allows for precise spatial control of biomaterials and cells, and incorporation of multiple design components, such as vasculature and cellular organization[5,41-43]. Further, customized bioreactor perfusion systems can facilitate the control and analysis of flow hemodynamics and culture conditions in the 3D cell cultures[44,45]. Combining these state-of-the-art technologies, the limitations of 2D cell culture and animal models can be conquered. Achieving a precise spatiotemporal control of the cells, tissues, and culture conditions enables accurate recapitulation of the native liver microenvironment.

1.2 3D Bioprinting

3D bioprinting is a form of additive manufacturing that uses a mixture of biocompatible materials, cells, and other biological reagents (e.g., growth factors) as bioink to create complex 3D structures that imitate natural tissue characteristics[43,46]. As this technology enables the fabrication of multicellular heterogenous tissues in a rapid, cost-effective, reproducible, and high-resolution manner[42,47], it has emerged as a promising

strategy to address the growing need for tissues and devices for *in vitro* disease modeling and drug screening, as well as in a variety of regenerative medicine applications[38,48].

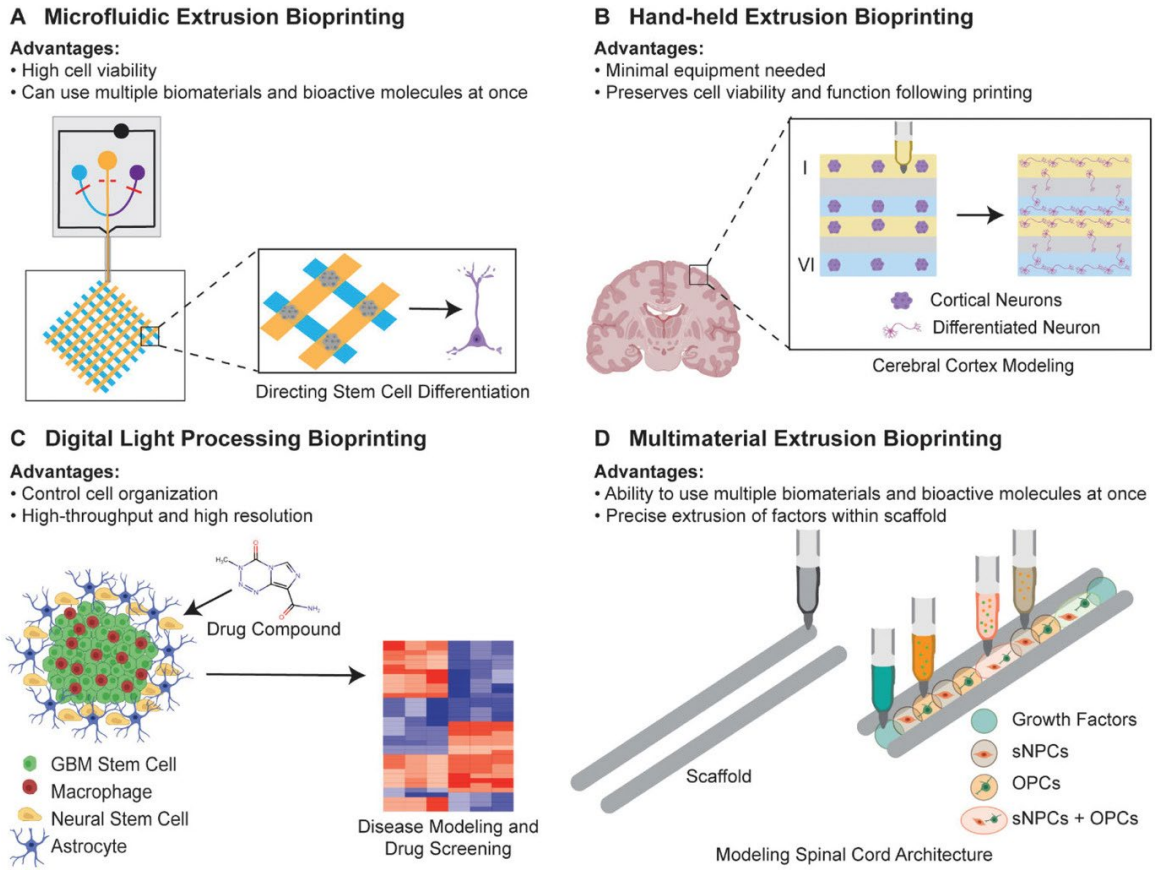

Figure 3. Different modalities of 3D bioprinting and their advantages. Adapted with permission[47]. Copyright © 2020 Wiley‐VCH GmbH.

Various modalities of 3D bioprinting have been developed, including extrusion-based, inkjet-based, laser-assisted, and stereolithography-based bioprinting (**Figure 3**)[49-51]. One of the most commonly used techniques is (micro)extrusion-based bioprinting, which utilizes a pneumatic dispensing system to extrude continuous bioink streams and allows layer-by-layer construction of the 3D structures[52,53]. In comparison to other 3D bioprinting techniques, extrusion bioprinters offer an outstanding advantage of incorporating multiple

biomaterials and bioactive factors at once[54]. Despite some limitations, such as moderate throughput, extrusion-based printing allows for maintaining high cell viability and function[49,55], and precise spatiotemporal control of various components in the 3D bioprinted constructs[47,56].

In this study, we utilized a multi-material extrusion-based 3D bioprinting approach to fabricate a 3D *in vitro* model of the human liver with a perfusable artery-like channel structure at a 20 μm resolution, for the study of hepatic function and fibrosis in response to dynamic microenvironmental conditions.

1.3 Aims of the Study

The objective of this study was to establish a 3D bioprinted, perfusable, *in vitro* model of the human liver for the study of liver fibrosis in response to altered ECM stiffness and flow conditions. Our central hypothesis was that bioprinted human liver constructs, consisting of functionalized hydrogel-based bioinks and human hepatocytes and ECs, can be used as a research-enabling platform to study the cellular mechanisms underlying hepatic dysfunction in liver fibrosis. To test this hypothesis, the following specific aims were pursued: **1)** To design, develop, and characterize biofabrication and culture conditions for constructing a vascular 3D human liver model; **2)** Determine the role of ECM stiffness in altering hepatic function and modeling liver fibrosis; and **3)** Evaluate the role of dynamic flow on hepatic function in healthy *vs.* fibrotic liver models. These conditions were introduced via a custom-designed bioreactor perfusion technology to create an *in vivo*-like liver microenvironment and examine the effect of flow hemodynamics.

Overall, this research aimed to establish a robust *in vitro* platform that helps to

decipher the hepatic cellular responses to microenvironmental alterations and their contributions to liver fibrosis. Further, the bioprinted model can serve as a high-throughput device to study a variety of factors as diagnostic and therapeutic targets of liver diseases for clinical applications.

CHAPTER 2. MATERIALS AND METHODS

2.1 Bioink Preparation

Gelatin methacrylate (GelMA) hydrogel was synthesized as an optimal biomaterial to prepare our bioink following the protocol described previously[57]. Briefly, gelatin from porcine skin (Sigma-Aldrich, USA) were mixed at 10% (w/v) into phosphate buffer saline (PBS, Sigma-Aldrich, USA) until fully dissolved. Subsequently, methacrylic anhydride (Sigma-Aldrich, USA) was added for gelatin modification at 50 °C. After 3 h of incubation, warm PBS was added for 15 min to stop the reaction. The mixture was dialyzed against Milli-Q water at 40 °C for 1 week to remove salts and methacrylic acid (with water being changed 2−3 times per day). The solution was then lyophilized (for 5−7 days) and stored away from light at −20 °C until use.

To prepare bioinks for printing, lyophilized gelMA was reconstituted in sterile PBS at a final concentration of 5% (w/v), mixed with 5% (w/v) gelatin and 0.5% (w/v) Irgacure (2-Hydroxy-4'-(2-hydroxye-thoxy)-2-methylpropiophenone, Sigma-Aldrich, USA). The gelMA-based bioink formulation was optimized with additional gelatin as a sacrificial material to reach target ECM stiffness and increase microporosity, and Irgacure as a photo initiator to facilitate efficient UV crosslinking. The pH of prepared gelMA-based bioinks was measured with a pH meter (FisherBrand, USA) and adjusted to 7.4 with 1N NaOH solution. pH balanced gelMA bioink was then stored away from light at 4°C before use for no longer than 2 weeks. 38% (w/v) Pluronic® F-27 (Sigma-Aldrich, USA) solution was prepared as the sacrificial bioink for bioprinting hollow structures in the designed model.

For printing cellular constructs, HepG2 cells (ATCC HB-8065, USA) were harvested at 90% confluency and uniformly suspended in pre-warmed gelMA bioink at 1×10^7 cells/mL. Cell-ladened bioinks were loaded into UV-sterilized printing syringes in the liquid state and stored at 4°C for 1 min for a rapid increase in viscosity (to enhance printability) before printing.

To prepare the bioinks for perfusion chamber casting, lyophilized gelMA was reconstituted in sterile PBS at a final concentration of 20% (w/v) with 0.5% (w/v) Irgacure. The pH of prepared gelMA-based bioinks was measured with a pH meter (FisherBrand, USA) and adjusted to 7.4 with 1N NaOH solution.

2.2 Design and 3D Bioprinting of Human Liver Models

3D human liver models were designed in Autodesk Fusion 360 computer-aided design (CAD) software (Autodesk, USA) and converted to the standard STL file format. The STL file was then sliced by Repetier (Hot-world GmbH & Co. KG, Germany), converted to G-Code, and implemented in a multi-headed 3D bioprinter (BioX, CELLINK, USA) for rapid and precise tissue manufacturing. Immediately after printing, constructs were crosslinked under ultraviolet (UV) light at a wavelength of 365 nm. To recapitulate the healthy *vs.* fibrotic liver tissue stiffness, bioprinted liver models were crosslinked at UV intensities of 5 mW/cm^2 *vs.* 40mW/ cm^2, respectively. Crosslinking was performed for 25s on both the top and bottom sides. Crosslinked constructs were subsequently transferred into the wells of 12- well tissue culture plates and cultured with pre-warmed HepG2 media in a humidified tissue culture incubator (37 °C, 5% CO_2).

2.3 Printing Fidelity Characterization

2.3.1 Printing Fidelity of Bioinks

A two-layer structure was designed to assess the fidelity of 3D bioprinting using 5% gelMA + 5% gelatin bioink. Bioprinted structures were crosslinked with UV at intensities of 5 mW/cm^2 and 40 mW/cm^2 for 50 s to compare the fidelity under two UV intensities used for bioprinted liver models (i.e., healthy *vs.* fibrotic tissues). 3D bioprinted layers were examined under an optical microscope (Leica Microsystems, DFC7000T, Germany) to assess printing fidelity using ImageJ (National Institutes of Health, USA). Four geometrical factors were quantified, including: strand diameter ratio (D_r), strand uniformity ratio (U_r), strand angle ratio (α_r), and interstrand area ratio (A_r).

A strand diameter ratio, D_r, was defined as the ratio of the diameter of the printed strand (D_p) to the diameter of the designed strand (D_d = 300 μm) in the CAD model:

$$D_r = \frac{D_p}{D_d} \tag{1}$$

Deformation of 3D bioprinted strands in the radial direction can be assessed with D_r. A high printing fidelity is determined when $Dr \approx 1$, while significant strand distortion is determined when $D_r \gg 1$ or $D_r \ll 1$.

A strand uniformity ratio, U_r, was defined as the ratio of the actual length of the printed strand (L_p) and the length of the designed strand (L_d = 9 mm) in the CAD model:

$$U_r = \frac{L_p}{L_d} \tag{2}$$

A nonuniform strand is identified when $U_r \gg 1$ or $U_r \ll 1$, while a uniform print is considered with $U_r \approx 1$.

A strand angle ratio, αr, was defined as the ratio of the actual inter strand angle of printed strand (α_p) and the designed angle (α_d = 60°) in the CAD model:

$$\alpha_r = \frac{\alpha_p}{\alpha_d} \tag{3}$$

The α_r parameter was used to quantify the misplacement and distortion of printed layers across two consecutive layers. As such, α_r values can illustrate a high printing fidelity with no layer misplacement when $\alpha_r \approx 1$, and a low structural fidelity when $\alpha_r \gg 1$ or $\alpha_r \ll 1$.

An interstrand area ratio, A_r, was defined to quantify the surface area of the quadrilateral openings created by four strands of two consecutive printed layers. A_r was determined by dividing the surface area of the actual printed quadrilateral opening (A_p) to that of the designed CAD model (A_d = 1 mm^2):

$$A_r = \frac{A_p}{A_d} \tag{4}$$

Th A_r parameter can demonstrate variation in both strand uniformity and strand angle. $A_r \approx 1$ indicates high fidelity, and $A_r \gg 1$ or $A_r \ll 1$ demonstrates low fidelity.

A total n = 3 two-layer constructs were 3D bioprinted for UV crosslinking intensities at both 5mW/cm^2 and 40mW/cm^2, respectively. Bright field microscopy images of randomly picked regions in each construct were acquired and measured manually.

2.3.2 Printing Fidelity of 3D human liver constructs

Acellular 3D human liver models (n = 3) were 3D bioprinted with 5% gelMA+5% gelatin bioinks and their bulk dimensions were measured to assess the macro-scale printing fidelity. The length, width, height, and channel diameter of the printed constructs were measured immediately post printing. Ratios of the four parameters to CAD designed values were calculated, respectively, to evaluate the printing fidelity of 3D human liver structure. A ratio $\gg 1$ or $\ll 1$ demonstrates low bulk fidelity, while a ratio of ≈ 1 indicates high printing fidelity.

2.4 Mechanical Testing

The elastic modulus of bioprinted liver constructs was measured by microindentation (Mach-1 V500C, Biomomentum, Canada). For this purpose, simplified cubic liver constructs were 3D bioprinted and cultured in static condition. A total n = 4 samples were measured for liver constructs in both healthy and fibrotic groups on days 2 and 14 post bioprinting, respectively. A 500 μm probe was used to indent the surface of the liver constructs. All indentations were performed at a depth of 200 μm at 4 μm/s, with 2 indentation points on both the top and bottom surfaces for each sample. The force-displacement unloading curves were recorded and used to measure the stiffness (S)

according to the slope of the linear trend line at 90-100% displacement. Reduced elastic modulus (E_r) and plane strain modulus (E) was derived using equations (5-8)[58]:

$$E_r = \frac{\sqrt{\pi}}{2\beta}\frac{S}{\sqrt{A(h_c)}} \tag{5}$$

where, β is a geometrical constant on the order of 1, S is the sample stiffness, and $A(h_c)$ is the projected contact area at the contact depth of h_c, which can be obtained from the equation below:

$$A(h_c) = 2\pi R h_c - \pi {h_c}^2 \tag{6}$$

where

$$h_c = h_{max} - \varepsilon\frac{P_{max}}{S} \tag{7}$$

where, h_{max} and P_{max} are the peak unloading displacement and peak unloading force, respectively, and ε is a constant with a value of 0.75 for the spherical probe[59].

The elastic modulus, E, can then be calculated using the following equation[58]:

$$\frac{1}{E_r} = \frac{(1-v^2)}{E} + \frac{1-v_i^2}{E_i} \tag{8}$$

where, v and v_i are the Poisson's ratio of tested material and the indenter tip material, respectively (both equal 0.5). E_i represents the elastic modulus of the probe with a value of 2 GPa. All mechanical tests were performed at room temperature (~23℃).

2.5 Cell Culture

HepG2 cells (an immortal human liver cell line) were seeded in T75 flasks (Sigma, Z707546, USA) and cultured in Eagle's Minimum Essential Medium (EMEM, ATCC 30-2003, USA), supplemented with 10% fetal bovine serum (FBS, Corning Life Sciences, USA) and 1% antibiotic-antimycotic solution (Corning Life Sciences, USA). HepG2 media was changed every 2 days and cell cultures were split t 1:5 when 90% confluency was reached. For cell passaging, HepG2 cells were washed with 10 mL sterile PBS and incubated with 2 mL of 0.05% Trypsin/EDTA (Invitrogen, USA) at 37°C for 5 min. Four mL of HepG2 Media was then added to the flask to fully detach cells by pipetting the solution up and down.

Human umbilical vein endothelial cells (HUVECs), expressing endogenous green fluorescent protein (GFP) were plated on T75 flasks and cultured in complete HUVEC Media (VascuLife VEGF Endothelial Medium Complete Kit, Lifeline Cell Technology, USA), supplemented with 1% antibiotic-antimycotic solution (Corning Life Sciences, USA). HUVEC media was changed every 2 days and cell cultures were split at 1:10 when 90% confluency was reached. For passaging, cells were washed with 10 mL sterile PBS and incubated with 1 mL of 0.05% Trypsin/EDTA at 37°C for 5 min. 2 mL of HUVEC media was then added to the flask to fully detach cells by pipetting the solution up and down.

For both cell types, cell detachment was visually observed and confirmed under an optical microscope connected to a camera (Leica Microsystems DFC7000T, Germany). Cell density and viability were determined by mixing the cell suspension at 1:1 with Trypan Blue solution (Invitrogen, USA) and counting cells using an automated cell counter (Bio-Rad, USA). Cells were cultured at 37°C and 5% CO_2.

2.6 Endothelialization of Printed Vasculature

The central channel in the liver construct was endothelialized by manually seeding HUVECs onto the vessel lumen. On day 2 after bioprinting, HepG2-ladened liver constructs were coated with Matrigel (1% v/v) in HepG2 media in preparation for cell seeding. Samples in static and rocking groups were coated with Matrigel for 2 h, and samples in perfusion group were coated overnight. Subsequently, 80 μL of HUVEC suspension with a concentration of 1×10^7 cells/mL were injected into the central channel of constructs and incubated at 37°C and 5% CO_2 for 2 h to allow full HUVEC attachment onto the channel walls. After 2 h, fresh coculture media (50% HepG2 media + 50% HUVEC media) was added to the wells for the coculture of HepG2 cells and HUVECs.

2.7 Cell Viability and Proliferation Analysis

Cell viability and proliferation in the 3D liver constructs ($n = 4$) were assessed using noninvasive AlamarBlue assay at serial time points throughout the 2-week culture period (days 2, 7, 14)[60-62]. Acellular bioprinted constructs were used as control. The AlamarBlue reagent (Bio-Rad, USA) was prepared as 10% (v/v) with fresh HepG2 or coculture media and added to each well of the culture plates containing liver constructs. Constructs were incubated with AlamarBlue reagent for 4 h at 37°C. Subsequently, 100 μL of the AlamarBlue mixture ($n = 3$) was collected from each well and loaded into a 96-well plate to measure absorbance at 550 and 600 nm wavelengths using a microplate reader (Synergy 2, BioTek, USA). AlamarBlue reduction % was calculated based on a previously established protocol, as a measure of cell viability and growth[60,63,64]. For the dynamic

culture, coculture media was mixed with AlamarBlue reagent (same ratio as above) and perfused in the liver constructs for 4 h.

2.8 Bioprofiling Analysis

Cell culture supernatants of the bioprinted constructs were collected (n = 4) from the culture wells at serial time points of culture (days 2, 7, and 14). Four hundred μL of sample supernatants were analyzed using NovaFlex Bioprofile 2 (NovaBiomedical, USA). Metabolite concentrations (glucose, glutamine, glutamate, and lactate), ion concentrations (K^+, Na^+, and Ca^{2+}), and pH values were measured in the media of each construct. The data were normalized to fresh media samples (n = 4) to demonstrate the production/consumption rate of metabolites and changes in pH and ion concentrations as a function of culture time. Culture media was changed every 2 days. Cumulative changes of metabolites were determined and compared across different groups to assess the cell activities in different groups. Rates of metabolite production/consumption were calculated by dividing the changes of metabolites by the time between media changes.

2.9 Evaluation of Hepatic Function

Hepatic function of the bioprinted constructs was evaluated by assessment of albumin secretion in the cell culture supernatants as well as immunohistochemical (IHC) analyses (see section 2.10). Cell culture supernatants of each group were collected (n = 4) at serial time points (days 7 and 14) during culture. Albumin secretion was assessed using a Human Albumin ELISA Kit (Enzyme-Linked Immunosorbent Assay, ab108788, Abcam, UK). Culture media was changed every 2 days. Cumulative changes of hepatic secretome

were determined and compared across different groups to demonstrate the changes of hepatic function during the 2-week culture period.

2.10 Immunohistochemical Analysis

Following a 2-weeks 3D culture, bioprinted liver constructs were washed with warm PBS for 5 min for 3 successive times, fixed with 4% formaldehyde solution for 30 min, and washed with PBS again for 5 min for 3 successive times. Fixed constructs were embedded in 4% agarose and sliced with a Vibratome machine (VT1200S, Leica Biosystems, Germany) to 200 μm slices. For permeabilization, the samples were soaked with 0.5% Triton-X 100 (Electron Microscopy Sciences, USA) for 30 min and blocked with 1% bovine serum albumin (BSA, EMD Millipore, USA) solution for 1 h. Each slice was stained with albumin to verify hepatic function, DAPI to stain nuclei, and CD31 for the hepatic vasculature, which can also distinguish HUVECs from HepG2 cells. The samples were immunostained using a primary antibody against human serum albumin (1:100, ab10241, Abcam) and CD31 (1:100, ab76533, Abcam) at 4°C overnight. Subsequently, the samples were incubated with Alexa Fluor 594 donkey anti-mouse (1:500) for albumin and Alexa Fluor 488 donkey anti-rabbit (1:500) for CD31 at 4°C overnight. Finally, the samples were counterstained with 4′,6-diamidino-2-phenylindole (DAPI, blue) and visualized using a confocal laser scanning microscope (FV1000, Olympus, Japan). Quantification of albumin signals was conducted using ImageJ software.

2.11 Dynamic Culture and Bioreactor Perfusion

To examine the effect of dynamic culture on 3D bioprinted liver models, we performed two experimental set-ups: **1)** rocking on an orbital shaker (IBI Scientific BBUAAUV1S, USA) at a speed of 50 RPM; and **2)** perfusion in a customized bioreactor system (Ismatec IPC Digital Peristaltic Pump ISM933, USA) at a flow rate of 1 mL/min. The flow rate was set as physiologically relevant to that of hepatic venous flow *in vivo*[65,66], whereas the rocking speed was calculated from it. For the rocking group, bioprinted liver constructs were cultured in static until day 3 to ensure initial cell attachment and growth. For the perfusion group, the constructs were cultured in static for 7 days to ensure HUVECs attachment, to form a relatively uniform endothelium, before connecting them to the perfusion system.

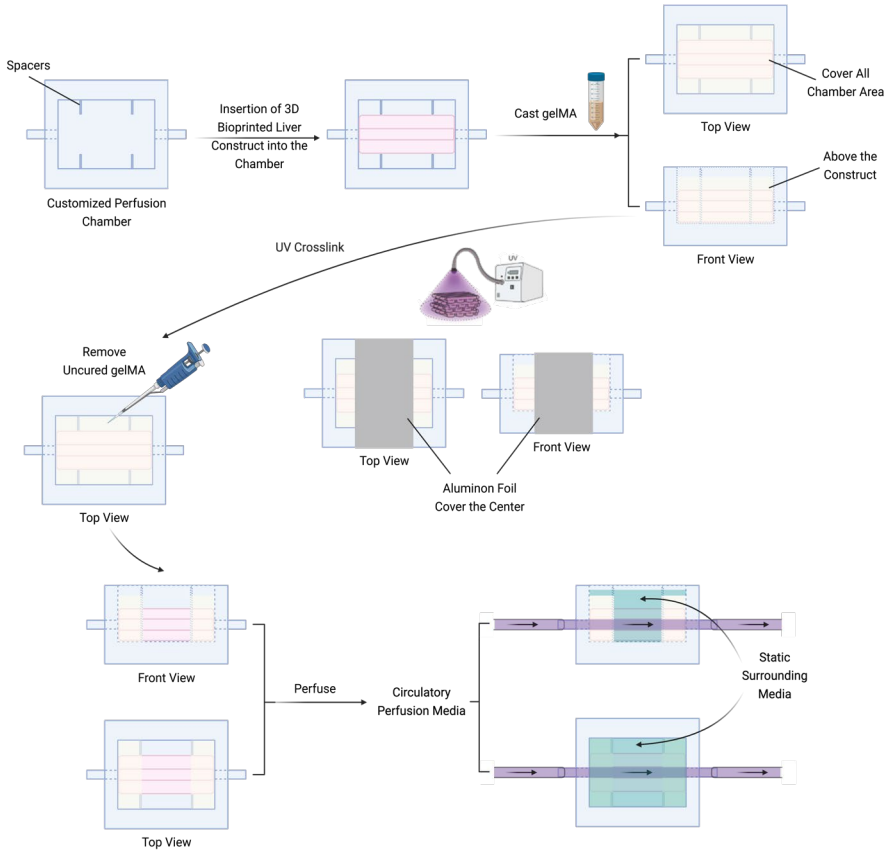

Figure 4. Schematic illustration of dynamic perfusion design. Components of the figure created with BioRender.com.

For the perfusion group, customized chambers were designed and 3D printed with a clear resin using a Form 3 SLA printer (Formlabs, USA) to closely fit the liver constructs. Isopropanol washes (30 min × 2) were used to remove residual resin, followed by drying, UV curing (20 min), and gluing the connector as post processing steps. A microscopic glass slide was used as a lid to cover and seal the open surface of the chamber, while allowing visual access to the embedded samples. Once transferred into the perfusion chambers, the constructs were immobilized with a 20 gauge needle (1/2", Nordson, USA) at the inlet and a 3D printed resin rod at the outlet. The perfusion chambers were then cast by 20% (w/v) gelMA and incubated at 37°C and 5% CO_2 for 30 min to ensure full sealing of the housed constructs. The central part of perfusion chambers was covered with Aluminum foil, and the whole chambers were cured under UV light at an intensity of 60 mW/cm^2 for 2 min. After UV curing, non-crosslinked gelMA was removed by pipetting, leaving a cavity at the central part of the chamber (**Figure 4**). By removing the rod at the outlet, the constructs in the perfusion chambers (n = 3) were connected to a 16-channel pre-sterilized perfusion system and perfused at 1mL/min for 1 day before a noninvasive AlamarBlue assay was conducted on days 8 along with the perfusion. At the end of perfusion culture, bioprinted constructs were harvested from perfusion chambers, washed with PBS, and fixed with 4% formaldehyde solution for further IHC analysis.

2.12 Statistical Analysis

Data for AlamarBlue and bioprofiling assays are presented as an average ± standard error of mean (SEM) for each time point. Significant differences were determined with

one-way ANOVA or two-way ANOVA (GraphPad Prism) if applicable. A post hoc Tukey-Kramer test was performed for multiple comparisons and a p-value of < 0.05 was considered statistically significant (*: p-value < 0.05, **: p-value < 0.01, ****: p-value < 0.0001). Samples sizes of at least $n = 4$ were used for each statistical analysis, including AlamarBlue, bioprofiling assays, and hepatic function evaluations. Least square means connecting letter reports were also used to show significant differences between multiple comparisons.

CHAPTER 3. RESULTS AND DISCUSSION

The objective of this study was to construct a 3D *in vitro* model of the human liver with a perfusable central channel for the study of liver fibrosis in response to altered ECM stiffness and dynamic microenvironmental conditions. The overall results showed that our 3D bioprinted model was a functional 3D *in vitro* human liver model that was able to: **1)** achieve the maintenance of high cell viability ($>$ 10% AlamarBlue reduction), exertion of key hepatic function (albumin secretion), and full vascular endothelialization throughout a 2-week culture period; **2)** attain the recapitulation of healthy *vs.* fibrotic states of human liver tissues through the alteration of ECM stiffness, and physiologically relevant flow conditions via the introduction of dynamic perfusion; and **3)** facilitate the elucidation of cellular mechanisms underlying liver fibrosis via the examination of cell proliferation and viability, metabolite consumption and production, hepatic function, and hepatocyte-EC interactions.

3.1 Bioprinting Fidelity

The printing fidelity of specific bioinks and 3D architectures can significantly influence the efficacy of manufacturing reproducible and consistent bioprinted constructs for high-throughput *in vitro* studies[67-71]. Thus, prior to the fabrication of 3D human liver models, the fidelity of 3D bioprinting using our gelMA-based bioink and the designed 3D liver structure were characterized at two different scales, i.e., the strand-level and bulk (macro)-level.

3.1.1 Printing Fidelity of Bioinks

Based on a two-layer construct, printing fidelity of the 5% (w/v) gelMA + 5% (w/v) gelatin bioink used in the bioprinting of 3D human liver models was assessed by measuring four parameters, strand angle (α), interstrand area (A), strand diameter (D), and strand uniformity (U) of the structure (**Figure 5**)[67]. Bioprinted constructs were crosslinked under UV at two intensities (5 mW/cm^2 and 40 mW/cm^2) in correspondence to those used for creating two levels of liver ECM stiffness. The fidelity of constructs post crosslinking was evaluated and compared between the two groups (n = 3). For both groups, relatively high fidelity was shown in strand angle and uniformity with α_r and $U_r \approx 1$, whereas interstrand area and strand diameter measurements indicated relatively low fidelity, with A_r and $D_r >$ 1.5. Significant differences ($p < 0.0001$) were observed in strand diameter and uniformity between constructs crosslinked at the two UV intensities (**Figure 5C**). Constructs crosslinked at the higher UV intensity presented a relatively higher fidelity with D_r and U_r approaching 1, suggesting the increase of gelMA crosslinking and rheological properties[57,72-74].

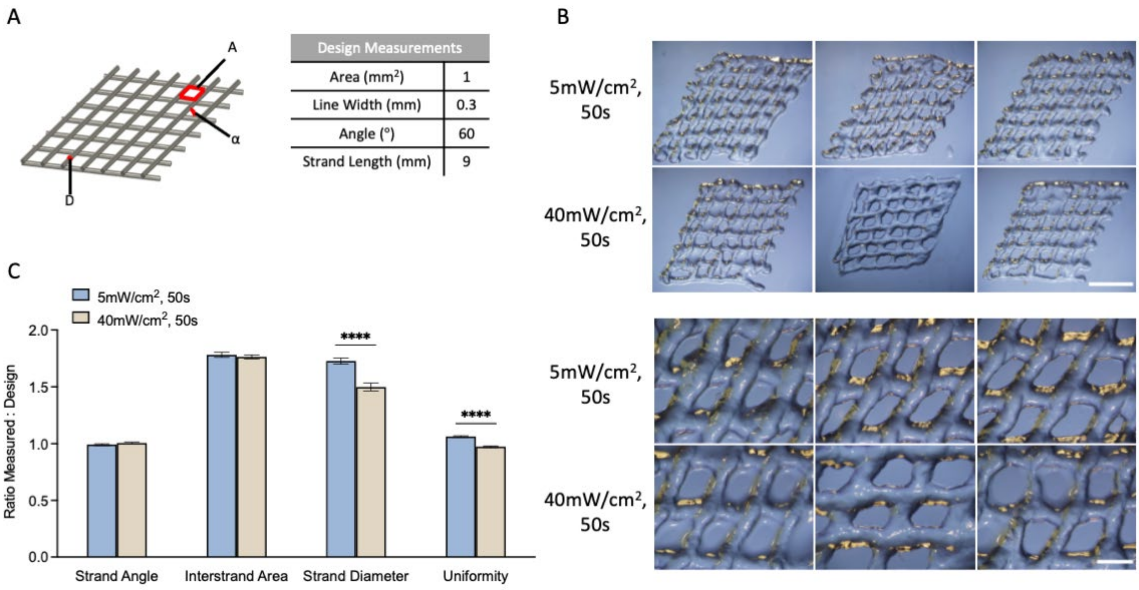

Figure 5. Characterization of printing fidelity of 5% (w/v) gelMA + 5% (w/v) gelatin bioink using 3D bioprinted two-layer structures. A: Numerical model of the two-layer construct used to assess fidelity by measuring printed strand angle (α), interstrand area (A), strand diameter (D), and strand uniformity (U). **B:** Bright field images of 3D bioprinted two-layer structures crosslinked using UV intensities of 5 and 40 mW/cm^2 for 50 s to recapitulate healthy *vs.* fibrotic liver tissue, respectively. Scale bar represents 1 mm. **C:** Quantitative analysis of strand angle ratio (α_r), interstrand area ratio (A_r), strand diameter ratio (D_r), and strand uniformity ratio (U_r) based on the images in panel (**B**). **** $p < 0.0001$. A total number of $n = 3$ was used for each group.

3.1.2 Macroscale Printing Fidelity of 3D human liver constructs

Next, the printing fidelity of the 3D human liver model was evaluated at the macro scale by measuring the ratios of four dimensions of 3D bioprinted liver constructs (length, width, height, and channel diameter), normalized to those of the CAD model (**Figure 6**)[47,67]. According to the measurements taken immediately post bioprinting, all four dimensions showed relatively high fidelity with all the ratios approaching 1 (**Figure 6C**). Small variations between replicates indicated high fidelity and reproducibility of our 3D bioprinted human liver model.

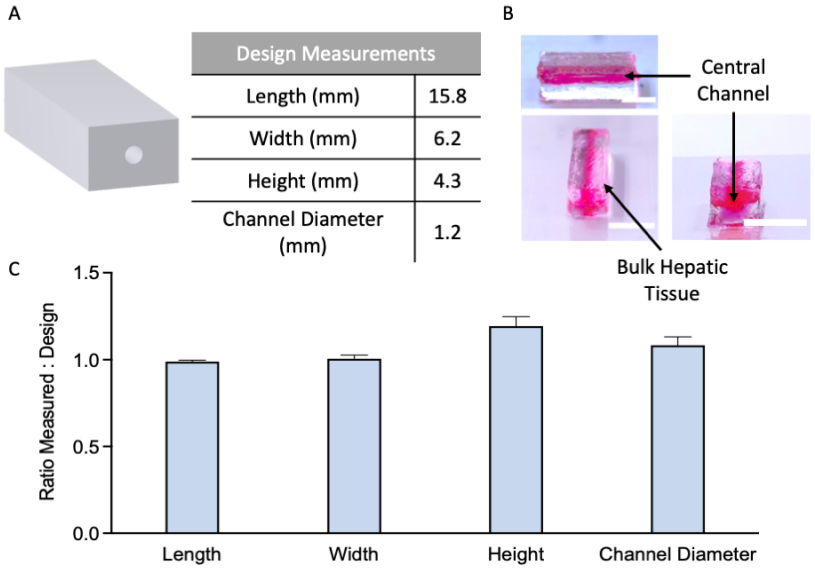

Figure 6. Characterization of 3D bioprinting fidelity of human liver model. A: CAD design of 3D human liver model. **B:** Optical images of 3D bioprinted human liver constructs for fidelity measurements. Scale bar represents 500 μm. **C:** Quantitative analysis of length, width, height and channel diameter based on the images as represented in panel (**B**) (n = 3).

3.2 Fabrication of 3D Bioprinted Liver Model

The 3D human liver model (**Figure 6A**) was bioprinted with a central artery-like channel (**Figure 6B**, arrows). Subsequently, bioprinted 3D liver constructs were UV crosslinked at two different intensities to modulate the ECM stiffness of the printed tissues. The resulting elastic moduli were determined using microindentation (**Figure 7A**).

Crosslinked cellular tissues were cultured with HepG2 media under static condition for 3 days to ensure cell attachment. Subsequently, various factors (i.e., cellular interactions and dynamic flows) were introduced to the 3D liver models (**Figure 7B**). For coculture groups, HUVECs were manually seeded into the channel lumen space within the constructs to achieve vascular endothelialization. An additional 4-day static culture was applied to the coculture perfusion group, to allow for full EC attachment, growth, and endothelialization, so that the cells can sustain the relatively aggressive dynamic flow conditions. During a total of 2-week culture, a variety of assessments were performed at serial time points to examine the cellular response and hepatic function of 3D human liver analogues. Assays included noninvasive AlamarBlue assay for the evaluation of cell viability and proliferation, quantitative bioprofiling analysis of culture supernatants to assess cellular metabolism and hepatic function, and IHC analysis to examine tissue structure and function (**Figure 7**).

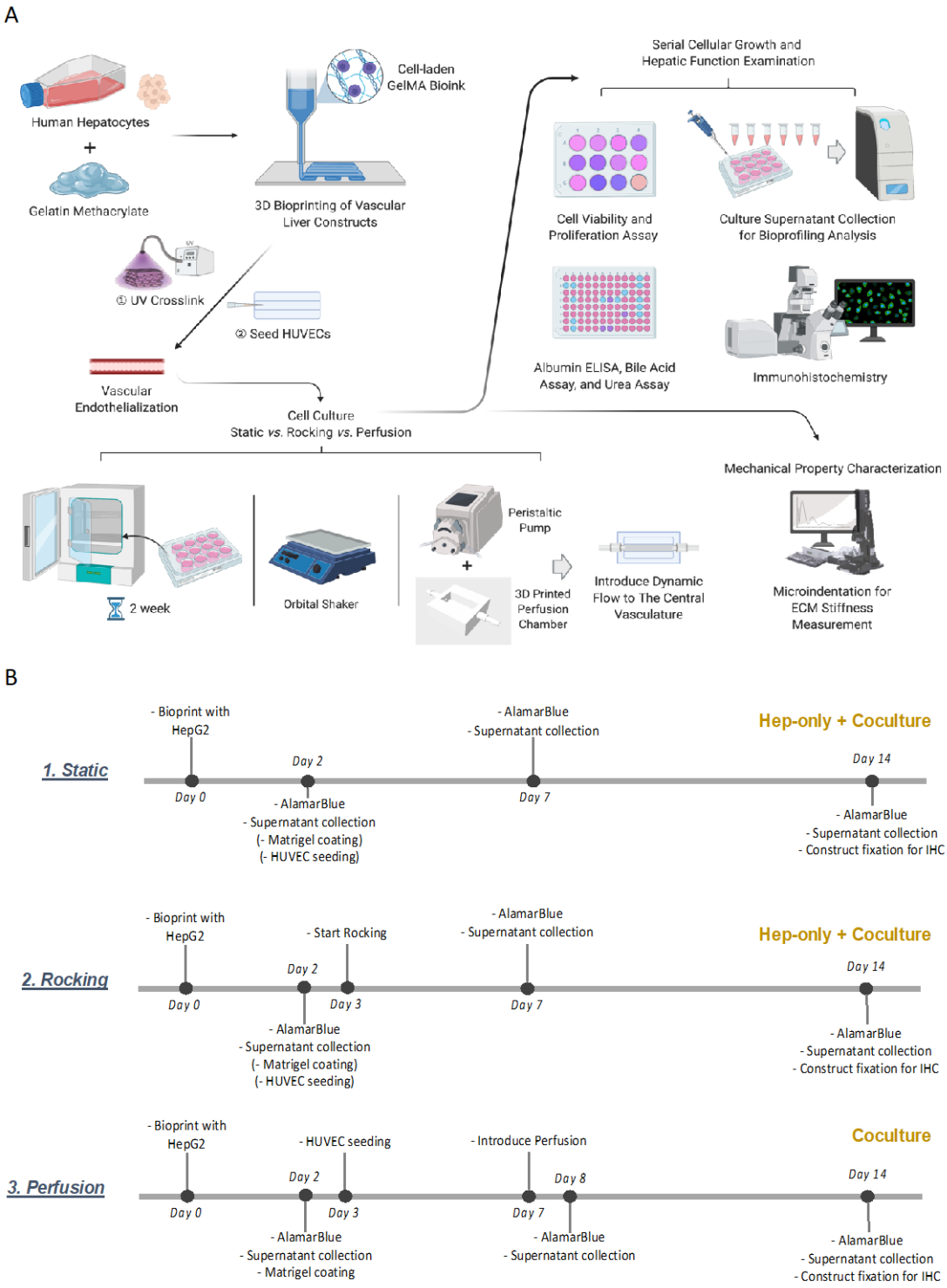

Figure 7. Summary of experimental design for the *in vitro* static versus dynamic culture of 3D bioprinted human liver analogues. A: Schematic illustration of the study workflow. **B:** The study timelines for the static, rocking, and perfusion groups, highlighting the key experimental steps for each study group. Components of the figure created with BioRender.com.

3.3 Simulating Liver Fibrosis through Modulating the Bioprinted Tissue Stiffness

To recapitulate the ECM stiffness of native human liver tissue at healthy (F0) *vs.* fibrotic (F4) states, a simplified cubic structure (**Figure 8A**) was designed and used for microindentation analysis to determine the elastic modulus of bioprinted constructs crosslinked at different UV intensities (**Figure 8B-C**). The simplified construct had the same height and width as the original 3D liver model, but 1/3 of the original length and no channel structure (to facilitate the microindentation testing). Meanwhile, since the simplified model had the same height and width as the original liver model, the UV crosslinking was performed identically in these two constructs and therefore, the same levels of elastic modulus could be expected from these models.

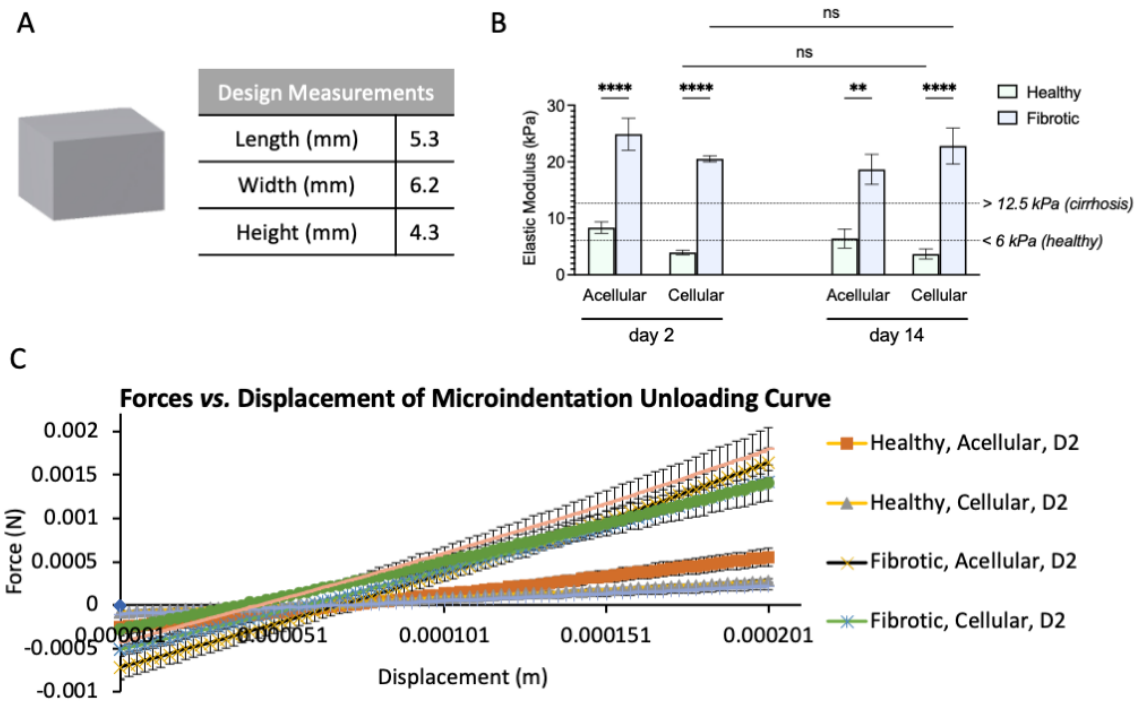

Figure 8. Elastic modulus measurement of 3D bioprinted liver constructs by microindentation. A: CAD design of simplified cubic model used for microindentation tests. **B**:

Elastic modulus of 3D bioprinted liver constructs crosslinked under UV at 5 *vs.* 40 mW/cm^2 for 50s to recapitulate physiologically relevant ECM stiffness of liver tissues in healthy *vs.* fibrotic states, respectively. **C**: Force *vs.* displacement curve for the microindentation unloading phase that was used for elastic modulus calculation. ** $p < 0.01$; and ****$p < 0.0001$. "ns" indicates non-significance ($n = 4$).

In addition to the comparison of elastic modulus between healthy and fibrotic groups, we also studied the effect of cellularization and time in culture on the bioprinted tissue stiffness (**Figure 8B-C**). Acellular and cellular liver constructs were both bioprinted and kept in HepG2 media at 37°C and 5% CO_2 for microindentation tests on days 2 and 14 after printing. The healthy and fibrotic liver stiffness values were successfully achieved with the elastic modulus of 2-4 kPa (F0) and 20-23 kPa (F4), respectively (**Figure 8B**)[20,75,76]. These results demonstrated high tunability of ECM stiffness in our 3D bioprinted gelMA-based platform, by optimizing bioink formulations and UV crosslinking conditions, to facilitate the characterization and modification of ECM mechanical properties. Additionally, acellular constructs showed a slightly higher elastic modulus as compared to cellular constructs under the same condition. This highlighted the effect of cell encapsulation in lowering ECM stiffness, which can be attributed to the cells' effect on decreasing the gelMA concentration, interfering with the UV crosslinking[77,78], and cell self-organization[79,80] and remodeling[81,82]. No significant differences were demonstrated between the measurements on days 2 and 14 in all groups, which indicates consistent ECM stiffness throughout the 2-week culture and successful maintenance of both the healthy and fibrotic states in our 3D human liver models.

3.4 Cell Viability and Proliferation

Noninvasive AlamarBlue assay was performed at serial time points to assess the cell viability and proliferation during the 2-week culture. Measuring AlamarBlue reduction is positively correlated with cell viability and growth, and a typical AlamarBlue reduction $> 10\%$ is considered appropriate for *in vitro* cultures[62,83].

Significant differences in AlamarBlue reduction were observed in hepatocyte-only constructs between healthy and fibrotic groups under the same condition (**Figure 9A**). While the healthy group presented high cell viability starting from day 2 and steady cellular growth until day 14, the fibrotic group demonstrated significantly lower cell viability at all time points. These results suggest the effect of healthy (F0) *vs.* fibrotic (F4) ECM stiffness as a critical liver microenvironmental cue, on hepatocytes viability and growth within bioprinted tissues. Further, the effect of dynamic flow on hepatocyte-only constructs was studied via the comparison between static and rocking conditions. By rocking the tissue culture plates on an orbital shaker at 50 RPM, a moderate dynamic flow was generated through the central vasculature (verified visually) and around the 3D liver constructs. While no significant differences were observed in healthy constructs between static and rocking groups, the fibrotic samples showed slightly lower cellular growth from day 2 to 7, as well as lower cell viability from day 7 to 14 (**Figure 9A**).

For the coculture studies, the healthy group sustained high cell viability throughout the 2-week culture, despite the moderate cellular growth after the introduction of HUVECs on day 3 (**Figure 9B**). In contrast, the fibrotic groups showed significant cellular growth on days 7 and 14, following HUVEC seeding. In comparison to the hepatocyte-only constructs, the coculture results suggested: **1)** possible preference of HUVECs to adhere and grow on/in higher-stiffness matrices; and **2)** increase of hepatocyte viability and

growth in fibrotic tissues possibly through hepatocyte-HUVEC interactions. However, as AlamarBlue reduction reflects the overall cell viability that is measured from supernatants in the 3D liver cultures, the cellular response specific to hepatocytes or HUVECs cannot be differentiated on days 7 and 14 in the cocultured constructs. Thus, additional assessment of cellular behavior must be conducted to evaluate the 3D coculture liver models. No significant influence of rocking condition was shown for the cocultured constructs (**Figure 9B**).

Overall, these results suggested that our 3D bioprinted human liver constructs: **1)** recapitulated cell viability and proliferation patterns of hepatocytes reported for healthy and fibrotic liver tissue *in vivo*[10,13,84,85]; **2)** supported the coculture of hepatocytes and HUVECs with high cell viability at both healthy and fibrotic ECM stiffness; **3)** exhibited consistent cell viability and proliferation rates in response to static and rocking conditions.

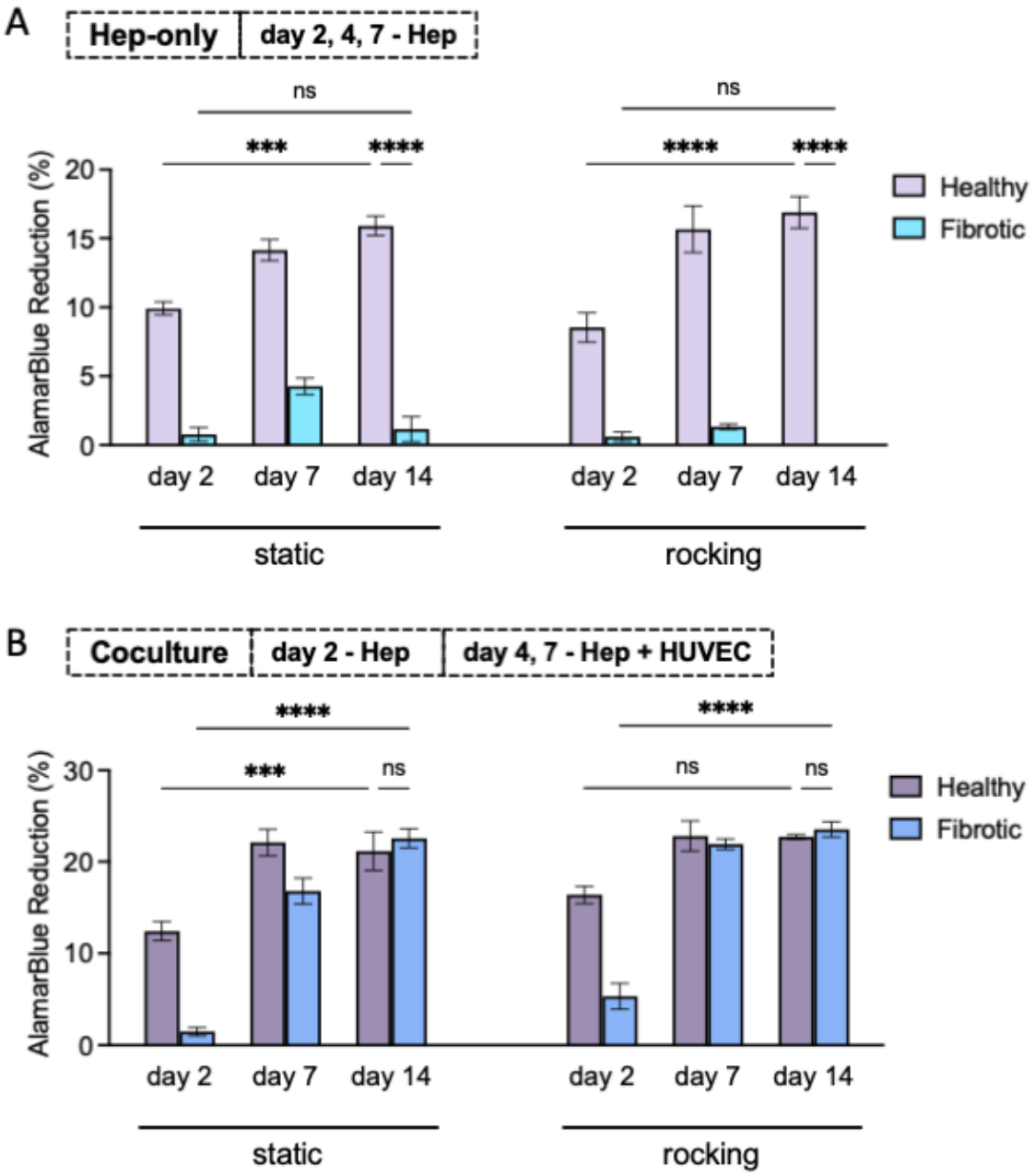

Figure 9. Cell viability and proliferation throughout the 2-week culture assessed by longitudinal AlamarBlue assay. A: AlamarBlue reduction of hepatocyte (Hep)-only constructs on days 2, 7, and 14 shows a steady increase in cell viability and growth, and significant differences between healthy and fibrotic groups. **B**: AlamarBlue reduction of coculture constructs on days 2, 7, and 14 showed a moderate cellular growth in healthy groups and a noticeable cellular growth in fibrotic groups after the introduction of HUVECs on day 3. *** $p < 0.001$; and **** $p < 0.0001$. "ns" indicates nonsignificance ($n = 4$).

3.5 Bioprofiling Analysis

Following the examination of cell viability and proliferation by AlamarBlue assay, the nutrient consumption and metabolite production during the 2-week culture were quantified via bioprofiling analysis (**Figure 10**). Changes of metabolite concentrations (glutamine, glucose, glutamate, and lactate) in the culture supernatants collected from each sample on days 2, 7, and 14 were compared over the 2-week culture span and across different groups for studying the effects of ECM stiffness, cellularization, and culture conditions on the metabolomic profile of hepatic cells.

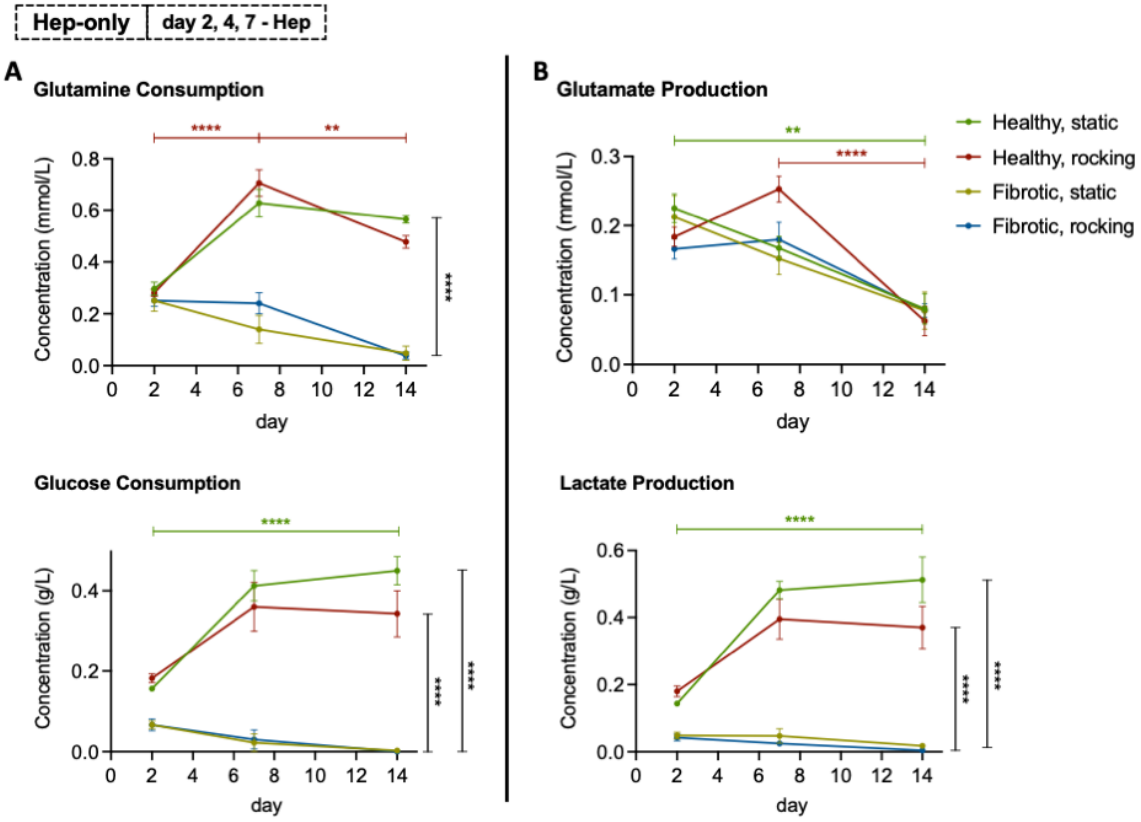

Figure 10. Metabolite production and nutrient consumption of hepatocyte (Hep)-only groups throughout the 2-week culture. A and **B:** Metabolomic bioprofiling analysis of metabolite

consumption (**A**) and production (**B**) in 3D cultured Hep-only samples. Results demonstrated significantly higher glucose/glutamine consumption (**A**) and lactate production (**B**) in healthy groups as compared to the fibrotic groups. **p < 0.01; ***p < 0.001; and ****p < 0.0001 (n = 4 per group).

For hepatocyte-only constructs, the glucose/glutamine consumption (**Figure 10A**) and lactate production (**Figure 10B**) were all significantly higher in the healthy groups than the fibrotic groups, which indicates a higher metabolic activity (glycolysis and glutamine metabolism) of hepatocytes in the 3D liver models[86-88]. Increase and decrease in metabolic activity were observed in healthy and fibrotic groups over time in culture, respectively, which is in agreement with the AlamarBlue results.

The overall differences in bioprofiling readouts for static and rocking conditions were not statistically significant (p > 0.05). However, for the healthy groups, rocking condition showed a slight decrease in cellular metabolism from days 7 to 14 in contrast to the continuous increase under static condition. In addition, a slight increase of glutamate production from days 2 to 7 followed by a significant drop from days 7 to 14 were observed under rocking condition (**Figure 10B**). As compared to the continuous decrease of glutamate production under static condition, these results suggest the possible contribution of rocking condition to the switch of metabolic patterns of hepatocytes[89,90].

For coculture constructs (**Figure 11**), cellular metabolism in the fibrotic groups was sustained and higher as compared to that in hepatocyte-only groups, which aligned well with the AlamarBlue results of elevated cell viability in cocultured fibrotic groups after HUVEC seeding (**Figure 9**). Relatively higher levels of glucose consumption (**Figure 11A**) and lactate production (**Figure 11B**) were obtained under rocking condition as

compared to static condition, which suggests the positive effect of dynamic culture (i.e., enhanced mass transport properties[91-93]) on cocultured liver models, especially at the fibrotic ECM stiffness. As such effect was not observed in hepatocyte-only constructs, it is possible that (1) HUVECs in the cocultured samples responded actively to the rocking condition, or (2) the cellular interactions between HUVECs and hepatocytes contributed to the amplified response of 3D human liver models to dynamic flow. Glutamine consumption also reflected the influence of rocking in a manner of metabolism fluctuation between days 2 to 7 and days 7 to 14, which again, could indicate a possible switch in metabolic pattern (**Figure 11A**). No significant differences were observed between different groups in glutamate production (**Figure 11A**).

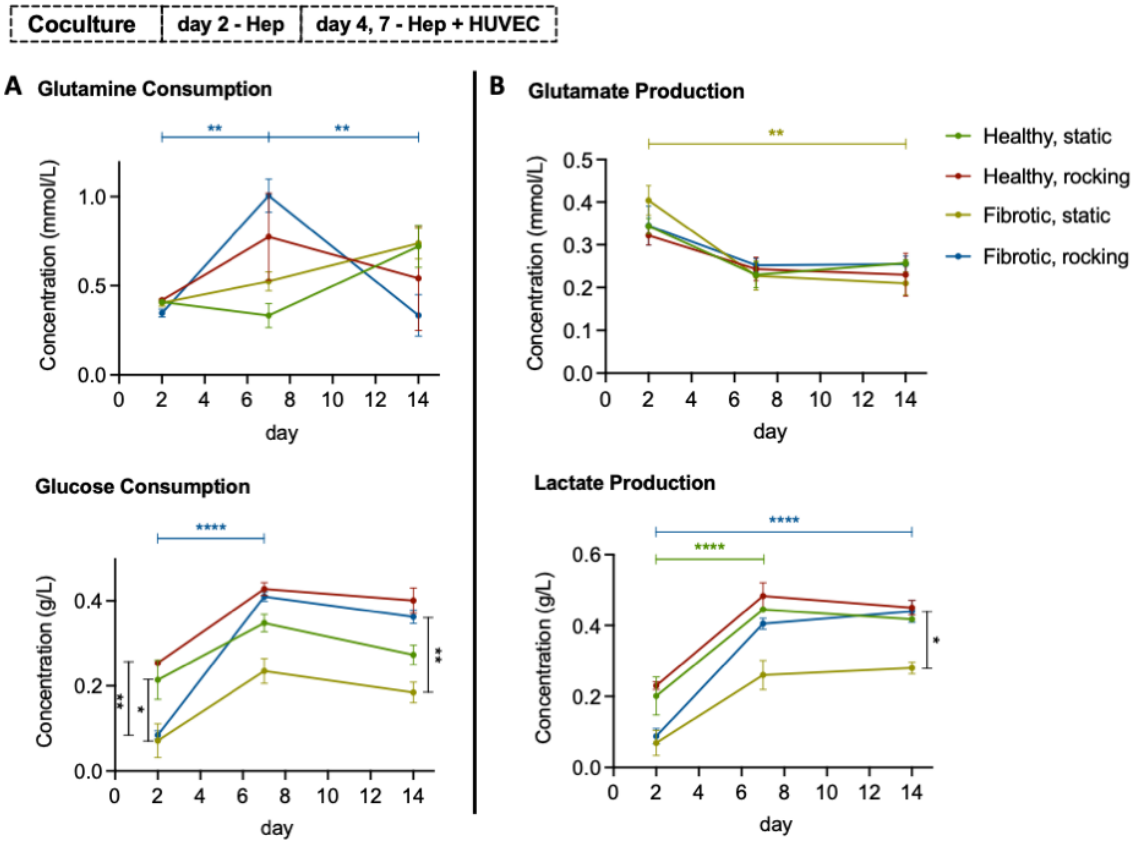

Figure 11. Metabolite production and nutrient consumption of coculture groups throughout the 2-week culture. A and **B:** Metabolomic bioprofiling analysis of metabolite consumption (**A**)

and production (**B**) in 3D cocultured groups. Significant increase of glucose consumption (**A**, bottom) and lactate production (**B**, bottom) were shown in fibrotic groups after HUVEC seeding. Higher metabolic activity was also demonstrated under rocking conditions in most groups. **p < 0.01; and ****p < 0.0001 ($n = 4$).

Overall, the bioprofiling results of both hepatocyte-only and coculture groups were in agreement with the longitudinal AlamarBlue results. Hepatocyte-only constructs showed significantly greater metabolic activity in the healthy groups than the fibrotic groups, which confirms successful recapitulation of liver fibrosis with ECM stiffness alterations. Coculture groups demonstrated an increase in overall cellular metabolism after the introduction of HUVECs, and higher metabolic activity under rocking condition as compared to that in static.

3.6 Evaluation of Hepatic Tissue Structure and Function

The hepatic tissue structure and function in 3D bioprinted constructs were evaluated in multiple ways via immunohistochemical analysis (to assess cell viability and growth, distribution, and function), ELISA assay (supernatant albumin quantification), and bright field microscopy for hepatocyte morphology and cluster examination.

3.6.1 Immunohistochemical Analysis of Tissue Structure and Function

For immunohistochemical analysis, 3D bioprinted liver constructs were harvested following 2 weeks of *in vitro* culture under varying conditions (static vs. dynamic flow) and stained with albumin (for hepatocytes), CD31 (for HUVECs), and DAPI for nuclei. Among all groups, the healthy hepatocyte-only group demonstrated the most *in vivo*-like hepatic features, including significant albumin expression and hepatocyte cluster formation

(**Figure 12**). Larger numbers and sizes of hepatocyte aggregations and cluster formations were observed around the outer wall region of liver constructs, which suggests the tendency of hepatocytes in our 3D models to self-organize, aggregate, and migrate towards superficial layers with higher nutrient/oxygen accessibility (**Figure 12**, white arrows). In addition, albumin expression was also shown to be positively correlated with the formation of hepatocyte clusters. The two features of hepatocytes can thus be identified as promising signs of cellular activity and hepatic function.

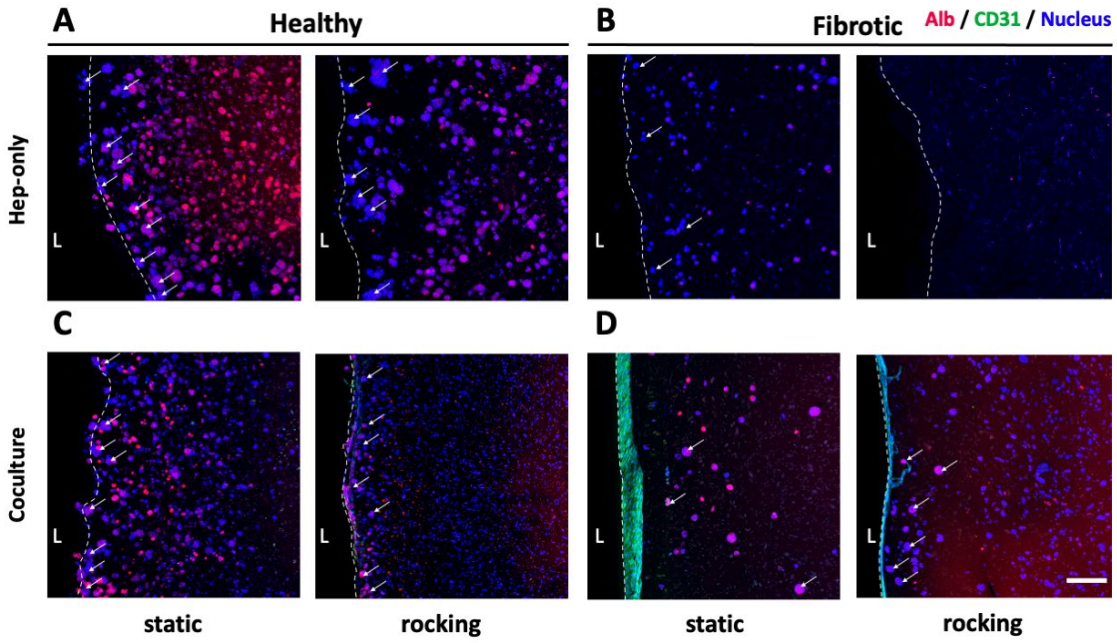

Figure 12. Immunohistochemical analysis of 3D bioprinted liver constructs performed after the 2-week culture. For both healthy (**A,C**) and fibrotic (**B,D**) groups, albumin (red) was used to assess hepatic function, CD31 (green) was used to label endothelial cells, and DAPI (blue) stained the nuclei. Significantly larger numbers and sizes of hepatocyte clusters were obtained in healthy hepatocyte-only group (**A**) compared to other groups (**B-D**). Fibrotic coculture group (**D**) demonstrated more robust HUVEC attachment to the outer wall of constructs compared to the healthy coculture group (**C**). Scale bar: 200 **μm**.

These results are in agreement with the AlamarBlue assay measurements and bioprofiling data presented in previous sections. In hepatocyte-only constructs, fibrotic (stiff) groups showed significantly lower albumin signal as compared to that of the healthy groups (**Figure 12A-B**). In contrast, there were no significant differences in hepatocyte distribution and albumin expression in the coculture constructs between healthy and fibrotic groups (**Figure 12C-D**). This suggests the effects of HUVECs in improving viability and function of hepatocytes[35,94,95]. Interestingly, a more robust HUVEC signal was observed around the external walls in the coculture fibrotic (stiff) group, while the coculture healthy group showed almost no HUVEC attachment at the outer wall (**Figure 12C-D**). This observation confirms, to some extent, our hypothesis (based on previous results) that higher printed tissue stiffness could favor the EC attachment and growth[96-98].

As for the comparison between static and rocking conditions, constructs under rocking condition showed less tissue integrity and albumin expression. Nonetheless, in the coculture groups, rocking conditions resulted in a more uniform hepatocyte distribution and albumin expression (**Figure 12C-D**). This could be partly attributed to the enhanced oxygen and nutrients transport within the rocking constructs in comparison to the static group. On the other hand, HUVECs overgrowth and formation of thick layers on the exterior surface (as observed in the coculture fibrotic groups) could significantly hamper the accessibility of hepatocytes to nutrients and oxygen. Therefore, further studies are needed to optimize the proportion and deposition of HUVECs and hepatocytes in these 3D bioprinted coculture systems.

Looking more closely into the printed vascular structures, IHC revealed promising evidence of uniform monolayered vascular endothelialization and extensive hepatocyte-

HUVEC interactions within the 3D bioprinted liver models after 2-week of culture (**Figure 13**). Of note, we observed some differences in the quantity of endothelial layers on the two opposite walls of these channels (**Figure 13A**, white arrows), which could be mainly attributed to the gravitational forces applied to seeded HUVECs, resulting in their preferential growth on the bottom side of the channels. We are currently working on improving EC distribution in these constructs by frequent (180 degree) flipping of the constructs post seeding. The cultured HUVECs also showed a degree of internal migration and remodeling towards the inner gelMA tissue (**Figure 13A**, yellow arrows) which would be a promising sign, increasing the chance of neo-angiogenesis for the longer-term cultures[99-101]. Together, these results demonstrate the great potential of this model to serve as a robust *in vitro* platform for future studies of a variety of factors, including hemodynamic changes in the central vasculature and cellular interactions in response to drugs and small molecules of interest.

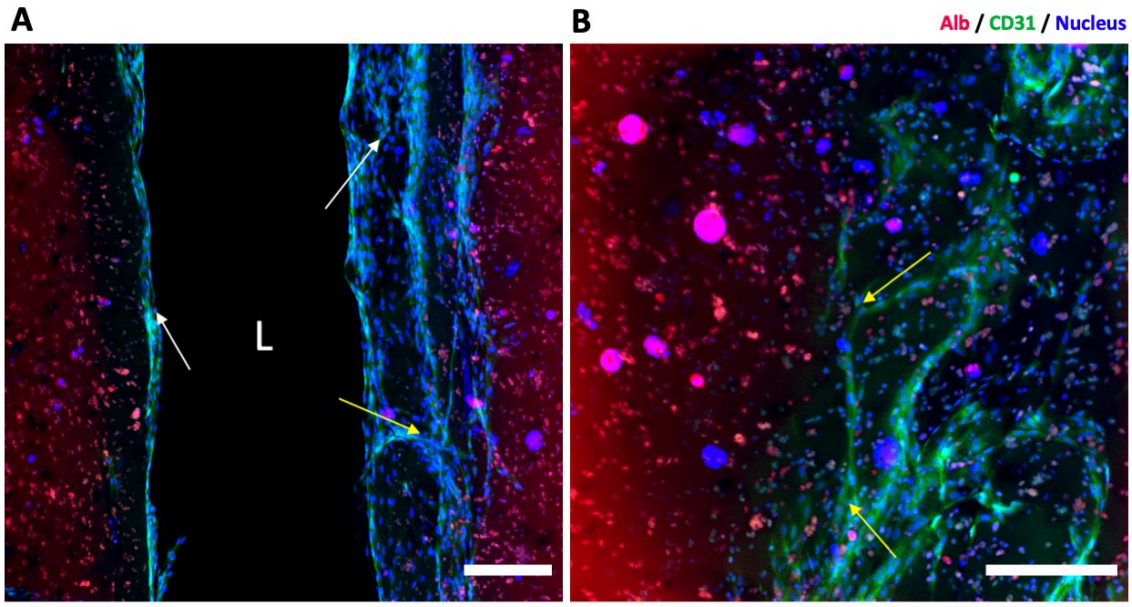

Figure 13. IHC images of fibrotic coculture group under static conditions, demonstrating hepatocyte-HUVEC interactions in 3D bioprinted constructs after a 2-week culture. Albumin (red) used to stain hepatocytes, CD31 (green) used to stain endothelial cells, and DAPI (blue) to stain nuclei. Full endothelialization of central vasculature (**A**) and extensive hepatocyte-HUVEC interactions (**B**) were achieved in our 3D bioprinted liver models. White arrows point to the relatively asymmetric distribution of HUVECs around the channel lumens. Yellow arrows highlight migration of HUVECs into the gelMA tissue. Scale bar: 200 **μm**.

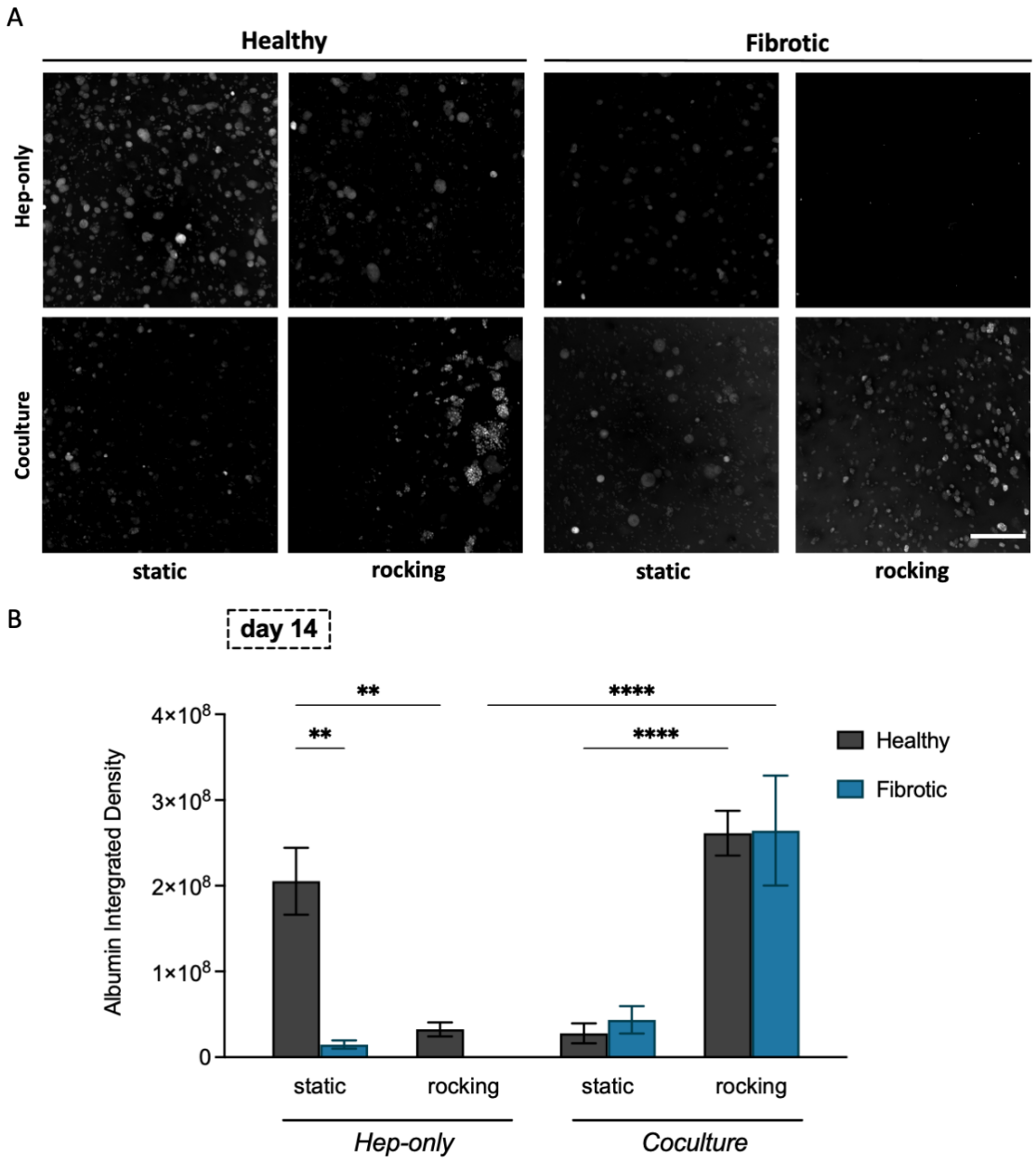

Figure 14. Immunofluorescent staining of human serum albumin in 3D bioprinted liver constructs performed after the 2-week culture. **A**: Representative IHC images of albumin staining for all experimental groups in this study. Scale bar: 200 **µm**. **B**: Quantification of total albumin signals shown in panel (**A**). Hepatocyte-only-healthy-static, coculture-healthy-rocking and coculture-fibrotic-rocking groups showed significantly higher albumin expressions compared to other groups (n = 5). **p < 0.01; ****p < 0.0001. to other groups (n = 5). **p < 0.01; ****p < 0.0001.

3.6.1.1 Immunofluorescence Quantification of Albumin within Bioprinted Tissues

The albumin expression within bioprinted hepatic tissues was further assessed via quantification of immunofluorescent signals of albumin in IHC images (**Figure 14**). Representative images of albumin staining in different groups were used (**Figure 14A**). A total $n = 5$ images from each experimental group were used for signal quantification. Results indicated significantly higher levels of albumin expression in healthy hepatocyte-only group under static condition, and the healthy- and fibrotic-coculture groups under rocking conditions (**Figure 14B**). The albumin signals in healthy-coculture-rocking group were mostly localized at the outer wall regions of constructs, which suggests an uneven hepatocyte distribution and function across the tissue, the preference of hepatocytes to aggregate near tissue edges, and potential errors in quantifying albumin expression due to spatial limitations for imaging.

3.6.2 Albumin Secretion

As a key hepatic function, albumin secretion of 3D bioprinted liver constructs was assessed by quantifying: **1)** the supernatant albumin via ELISA assay; and **2)** the albumin within scaffolds (intra and extra cellular albumin) using IHC analysis.

3.6.2.1 Supernatant Albumin Quantification

The albumin secreted by hepatocytes to the culture media was quantified on days 7 and 14 of culture and compared across different groups. Significantly higher levels of albumin secretion were obtained in the hepatocyte-only-healthy groups under both static and rocking conditions (**Figure 15**). All groups were able to maintain consistent albumin

secretion on days 7 and 14, which showed the stability of our 3D bioprinted liver model to sustain hepatic function over a two-week time span.

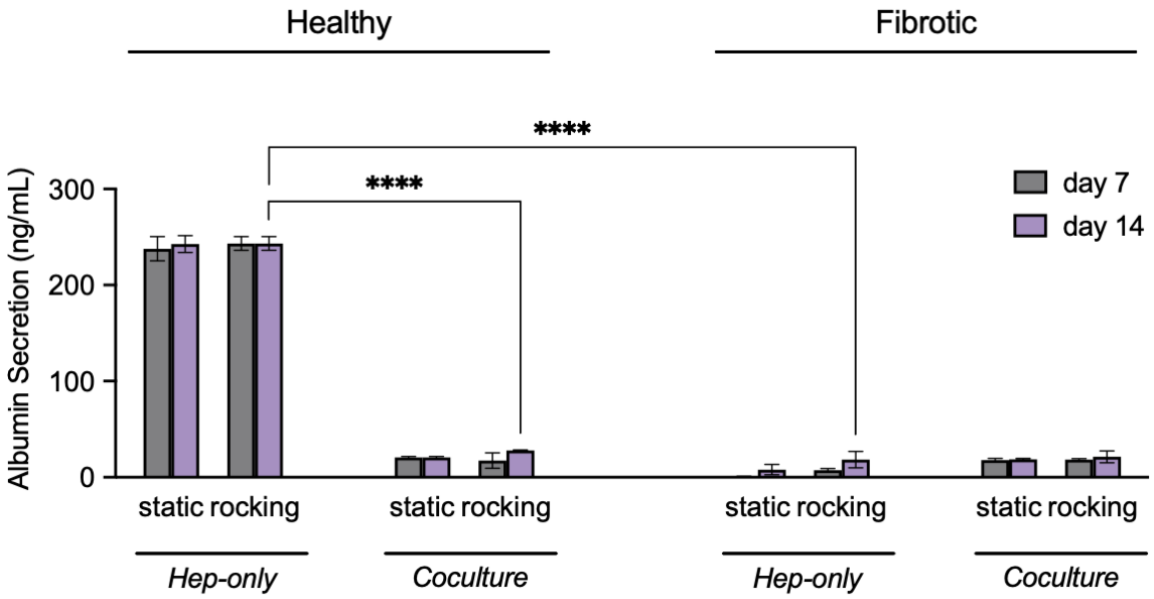

Figure 15. Albumin secretion into supernatants quantified on days 7 and 14 of *in vitro* culture to assess the hepatic function of 3D bioprinted liver model. The healthy tissue, containing hepatocyte cells only, showed the highest levels of albumin in the supernatant, in both static and rocking conditions. In other study groups, rocking resulted in an increase in albumin readouts, especially at day 14 of culture. ****$p < 0.0001$ ($n = 4$).

Comparing the two albumin quantification methods, we determined that the hepatocyte-only-heathy-static group showed the highest levels of albumin content in both culture media and within the tissues, which suggests greater hepatic function and albumin diffusion in this group. In contrast, the hepatocyte-only-healthy-rocking group demonstrated markedly lower albumin expression. Coculture-healthy-rocking and coculture-fibrotic-rocking groups presented much higher albumin expression inside hepatic tissues compared to that in the supernatants. As our previous results suggest

improvement of hepatocyte viability and function in coculture/rocking groups, it is possible that HUVEC attachment to the construct surfaces hindered the albumin diffusion and contributed to the albumin level variance between culture media supernatant and inside tissues.

3.6.3 Hepatocyte Cluster Formation

Hepatocyte cluster formation is considered as a positive indicator of hepatic cell viability and function. We, therefore, examined the formation of hepatocyte clusters via bright field microscopy on days 2 and 14 of culture (**Figure 16**). A remarkable cluster formation of hepatocytes was observed from days 2 to 14 in hepatocyte-only-healthy groups under both static and rocking conditions, as well as in the coculture-healthy-static group. These results are consistent with our previous observations in the sections above, which indicated higher cell viability and hepatic function in hepatocyte-only-healthy groups. Specifically, for healthy-rocking groups, the formation of hepatocyte clusters was diminished in the coculture group compared to the hepatocyte-only group. This suggests the effect of coculture (introducing ECs) on hepatocyte activities. Further studies would be required to examine the key players and cellular mechanisms underlying these phenomena.

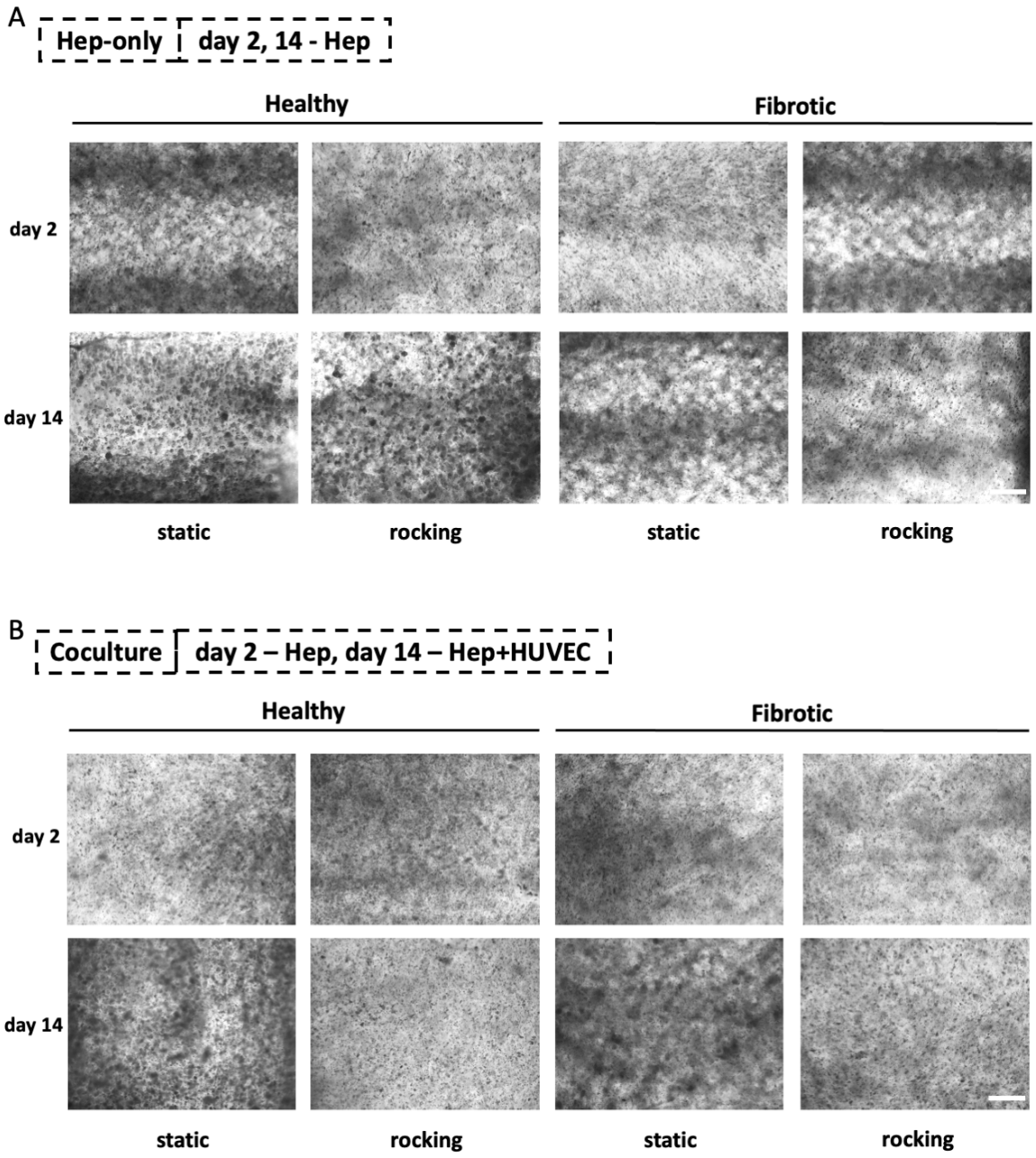

Figure 16. Representative bright field microscopy images of 3D bioprinted liver constructs at days 2 and 14 post bioprinting. Analyses were conducted on hepatocyte-only (**A**) and coculture (**B**) groups under static *vs.* rocking culture conditions. Substantial cluster formation of hepatocytes was observed at days 2 through 14 in hepatocyte-only-healthy-static, hepatocyte-only-healthy-rocking, and coculture-healthy-static groups. Scale bar: 50 μm (n = 4).

3.7 Dynamic Perfusion of 3D Bioprinted Liver Tissue Analogues

As the last experimental step of this study, dynamic perfusion was introduced through the central vasculature of our 3D coculture liver models (**Figure 17A-B**). Constructs containing hepatocytes and HUVECs at healthy *vs.* fibrotic ECM stiffness (n = 4) were cocultured in static until day 7 for initial cell attachment and proliferation. Subsequently, we transferred cellular constructs into custom-printed perfusion chambers. Following insertion of constructs in the chamber, we sealed the inlet and outlet regions via casting and crosslinking 20% gelMA solution (**Figure 17B**). The perfusion chamber was then connected to a peristaltic bioreactor system (**Figure 17A**). A physiologically relevant flow rate of 1 mL/min (based on literature[65,66,102]) was applied to perfuse the coculture constructs. As the setup was originally designed to allow for culture media exchange in the chamber cavity, a removable lid was initially used as shown in **Figure 17A**. However, due to the relatively low resistance created by microporosity in our cell-ladened gelMA constructs, the diffusion of culture media to the chamber cavity was rapid and tended to cause leakage problems. Thus, alternatively, a glass slide was permanently glued to the top of perfusion chamber to enable fully sealed media perfusion through the central vasculature, while still allowing for cavity space for static media in the perfusion chambers (**Figure 17B**).

Coculture constructs with healthy and fibrotic stiffness were cultured in the dynamic perfusion for another 8 days. A noninvasive AlamarBlue assay was performed on days 2 and 8 of dynamic culture to assess the cell viability (**Figure 18**). Results demonstrated that the hepatocyte-HUVEC cell viability was successfully maintained in 3D liver constructs under flow. Consistent with previous results, the fibrotic groups showed

an increase of AlamarBlue reduction from days 2 to 8, possibly due to the HUVECs activities. Although the cell viability and growth were not high in this coculture perfusion group, it provided promising insights for our 3D liver models to sustain cell viability, tissue integrity, and hepatic function under physiologically relevant flow conditions. Future works will focus on further optimization of perfusion setups to achieve a more stable and long-term perfusion culture.

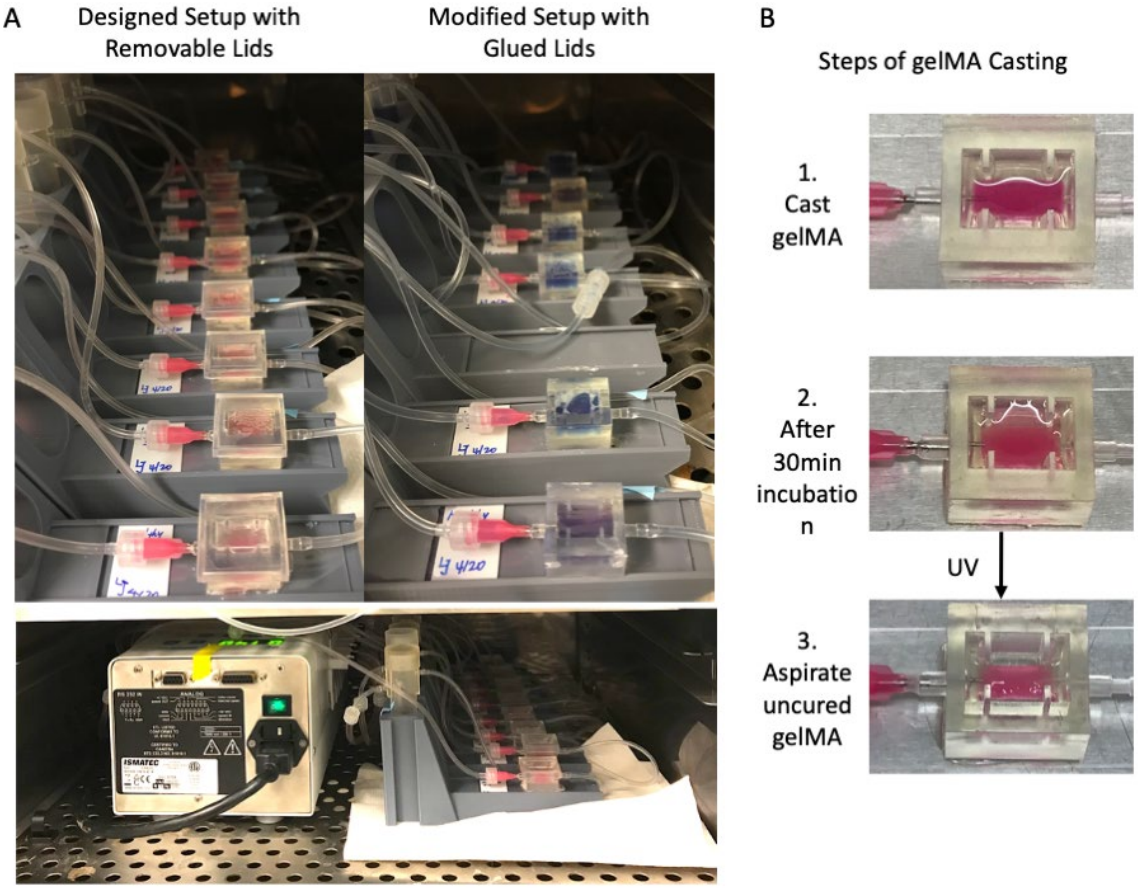

Figure 17. Setup of the custom-designed perfusion system used for dynamic culture of bioprinted liver constructs. A: Housed 3D liver constructs were connected to a peristaltic pump and perfused at a flow rate of 1 mL/min. **B**: Steps followed for gelMA casting to seal the inlet and outlet of liver constructs while leaving an accessible space on top of the construct for the media exchange in central parts of the chamber.

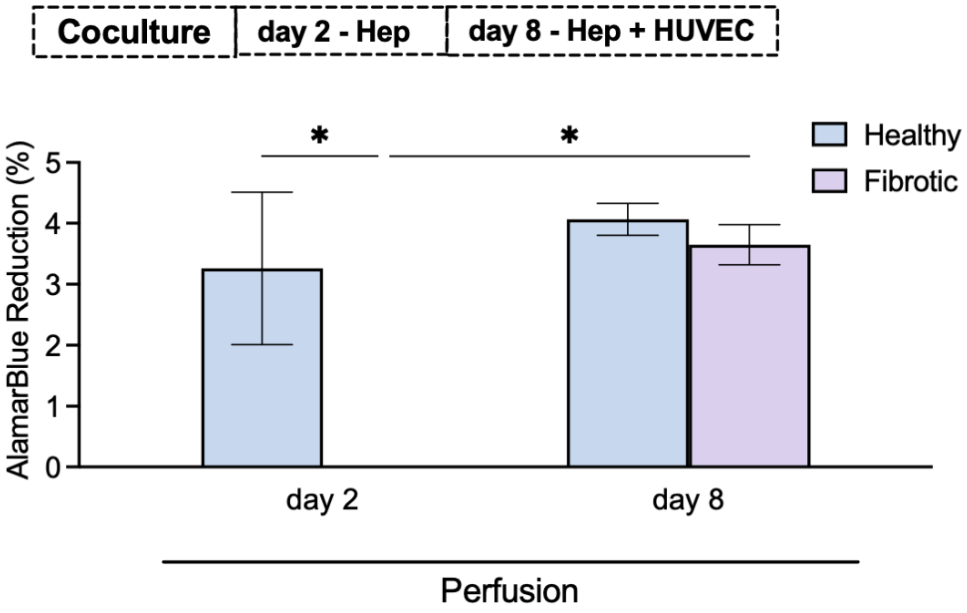

Figure 18. Noninvasive quantification of cell viability and proliferation in coculture/perfusion groups assessed by AlamarBlue assay. Following 7 days of static culture (to ensure cells attachment and settling), we conducted 8 days of dynamic flow at 1 mL/min. AlamarBlue results demonstrated adequate cell viability and growth within the 8-day dynamic flow period.

CHAPTER 4. CONCLUSIONS

In this study, we established a 3D bioprinted, perfusable human liver model that successfully recapitulated the native liver tissue microenvironmental cues for healthy *vs.* fibrotic states by the modulation of ECM stiffness. Engineered liver models retained viability, proliferation, and function of both human endothelial and hepatic cells during a 2-week culture period. Further, we studied the effect of hepatocyte-HUVEC coculture and dynamic flow conditions (static *vs.* rocking) in our 3D bioprinted model of liver fibrosis. We examined cell viability and proliferation, nutrient consumption and metabolite production, cellular organization, and hepatic function in the 3D liver models at serial time points during culture. Results collectively demonstrate that relatively high levels of cellular growth and hepatic function can be achieved in hepatocyte-only liver models at healthy ECM stiffness. Meanwhile, promising vasculature endothelialization and cellular interactions were presented in coculture liver models at fibrotic ECM stiffness. Finally, a pilot coculture perfusion study was successfully conducted using a customized bioreactor system, demonstrating the robust potential of this 3D bioprinted liver platform to be utilized for intensive *in vitro* studies of liver diseases.

Nevertheless, in this study, the hepatic function of 3D bioprinted liver constructs was mainly indicated by albumin secretion and hepatocyte cluster formation, further gene expression or immunohistochemical analysis could be performed to examine the hepatic structure, function more distinctly, and hepatocyte-HUVEC interactions more comprehensively. To elucidate the impact patterns of dynamic flows and hepatocyte-HUVEC coculture on the 3D liver models, additional experiments may be conducted to clarify the results.

In summary, here we demonstrated a promising 3D bioprinted human liver model for the study of liver fibrosis *in vitro*. Future directions of this research could further explore and modulate the dynamic perfusion and hepatocyte-HUVEC interactions in this platform for optimal hepatic function. Various factors of interest could also be incorporated to the model for disease modeling and drug screening applications in high throughput manners.

REFERENCES

1. Friedman SL. Liver fibrosis -- from bench to bedside. *J Hepatol.* 2003;38 Suppl 1:S38-53.

2. Ginès P, Cárdenas A, Arroyo V, Rodés J. Management of cirrhosis and ascites. *N Engl J Med.* Apr 15 2004;350(16):1646-1654.

3. Hernandez-Gea V, Toffanin S, Friedman SL, Llovet JM. Role of the microenvironment in the pathogenesis and treatment of hepatocellular carcinoma. *Gastroenterology.* Mar 2013;144(3):512-527.

4. Rychik J. The Relentless Effects of the Fontan Paradox. *Semin Thorac Cardiovasc Surg Pediatr Card Surg Annu.* 2016;19(1):37-43.

5. Ma L, Wu Y, Li Y, et al. Current Advances on 3D-Bioprinted Liver Tissue Models. *Advanced Healthcare Materials.*n/a(n/a):2001517.

6. Blachier M, Leleu H, Peck-Radosavljevic M, Valla D-C, Roudot-Thoraval F. The burden of liver disease in Europe: A review of available epidemiological data. *Journal of Hepatology.* 2013/03/01/ 2013;58(3):593-608.

7. Asrani SK, Devarbhavi H, Eaton J, Kamath PS. Burden of liver diseases in the world. *J Hepatol.* Jan 2019;70(1):151-171.

8. Yang JD, Hainaut P, Gores GJ, Amadou A, Plymoth A, Roberts LR. A global view of hepatocellular carcinoma: trends, risk, prevention and management. *Nature Reviews Gastroenterology & Hepatology.* 2019/10/01 2019;16(10):589-604.

9. Aydın MM, Akçalı KC. Liver fibrosis. *Turk J Gastroenterol.* Jan 2018;29(1):14-21.

10. Guyot C, Lepreux S, Combe C, et al. Hepatic fibrosis and cirrhosis: the (myo)fibroblastic cell subpopulations involved. *Int J Biochem Cell Biol.* Feb 2006;38(2):135-151.

11. Correale M, Tarantino N, Petrucci R, et al. Liver disease and heart failure: Back and forth. *Eur J Intern Med.* Feb 2018;48:25-34.

12. Zhang CY, Yuan WG, He P, Lei JH, Wang CX. Liver fibrosis and hepatic stellate cells: Etiology, pathological hallmarks and therapeutic targets. *World J Gastroenterol.* Dec 28 2016;22(48):10512-10522.

13. Kisseleva T, Brenner D. Molecular and cellular mechanisms of liver fibrosis and its regression. *Nature Reviews Gastroenterology & Hepatology.* 2021/03/01 2021;18(3):151-166.

14. Fede G, Privitera G, Tomaselli T, Spadaro L, Purrello F. Cardiovascular dysfunction in patients with liver cirrhosis. *Ann Gastroenterol.* Jan-Mar 2015;28(1):31-40.

15. Iwakiri Y. Pathophysiology of portal hypertension. *Clin Liver Dis.* May 2014;18(2):281-291.

16. Roehlen N, Crouchet E, Baumert TF. Liver Fibrosis: Mechanistic Concepts and Therapeutic Perspectives. *Cells.* 2020;9(4):875.

17. Bataller R, Brenner DA. Liver fibrosis. *J Clin Invest.* Feb 2005;115(2):209-218.

18. Wilder J, Patel K. The clinical utility of FibroScan(®) as a noninvasive diagnostic test for liver disease. *Med Devices (Auckl).* 2014;7:107-114.

19. Fitzpatrick E, Quaglia A, Vimalesvaran S, Basso MS, Dhawan A. Transient elastography is a useful noninvasive tool for the evaluation of fibrosis in paediatric chronic liver disease. *J Pediatr Gastroenterol Nutr.* Jan 2013;56(1):72-76.

20. Mueller S, Sandrin L. Liver stiffness: a novel parameter for the diagnosis of liver disease. *Hepat Med.* May 25 2010;2:49-67.

21. Foucher J, Chanteloup E, Vergniol J, et al. Diagnosis of cirrhosis by transient elastography (FibroScan): a prospective study. *Gut.* Mar 2006;55(3):403-408.

22. Nevzorova YA, Boyer-Diaz Z, Cubero FJ, Gracia-Sancho J. Animal models for liver disease – A practical approach for translational research. *Journal of Hepatology.* 2020;73(2):423-440.

23. Liu Y, Meyer C, Xu C, et al. Animal models of chronic liver diseases. *American Journal of Physiology-Gastrointestinal and Liver Physiology.* 2013;304(5):G449-G468.

24. Lin C, Khetani SR. Advances in Engineered Liver Models for Investigating Drug-Induced Liver Injury. *Biomed Res Int.* 2016;2016:1829148.

25. Xiang C, Du Y, Meng G, et al. Long-term functional maintenance of primary human hepatocytes in vitro. *Science.* 2019;364(6438):399-402.

26. Wang Y, Jiang J. A two-dimensional (2D) systems biology-based discrete liver tissue model: A simulation study with implications for ultrasound elastography of liver fibrosis. *Comput Biol Med.* Jan 2019;104:227-234.

27. Sadasivan SK, Siddaraju N, Khan KM, et al. Developing an in vitro screening assay platform for evaluation of antifibrotic drugs using precision-cut liver slices. *Fibrogenesis & Tissue Repair.* 2015/01/09 2015;8(1):1.

28. Jucker M. The benefits and limitations of animal models for translational research in neurodegenerative diseases. *Nature Medicine.* 2010/11/01 2010;16(11):1210-1214.

29. Geerts A. History, heterogeneity, developmental biology, and functions of quiescent hepatic stellate cells. *Semin Liver Dis.* Aug 2001;21(3):311-335.

30. van de Bovenkamp M, Groothuis GMM, Meijer DKF, Slooff MJH, Olinga P. Human liver slices as an in vitro model to study toxicity-induced hepatic stellate cell activation in a multicellular milieu. *Chem Biol Interact.* Jul 25 2006;162(1):62-69.

31. Mitaka T, Sato F, Mizuguchi T, Yokono T, Mochizuki Y. Reconstruction of hepatic organoid by rat small hepatocytes and hepatic nonparenchymal cells. *Hepatology.* Jan 1999;29(1):111-125.

32. Karam WG, Ghanayem BI. Induction of replicative DNA synthesis and PPAR alpha-dependent gene transcription by Wy-14 643 in primary rat hepatocyte and non-parenchymal cell co-cultures. *Carcinogenesis.* Nov 1997;18(11):2077-2083.

33. Shimaoka S, Nakamura T, Ichihara A. Stimulation of growth of primary cultured adult rat hepatocytes without growth factors by coculture with nonparenchymal liver cells. *Exp Cell Res.* Sep 1987;172(1):228-242.

34. Ries K, Krause P, Solsbacher M, et al. Elevated expression of hormone-regulated rat hepatocyte functions in a new serum-free hepatocyte-stromal cell coculture model. *In Vitro Cell Dev Biol Anim.* Sep 2000;36(8):502-512.

35. Villafuerte BC, Koop BL, Pao CI, Gu L, Birdsong GG, Phillips LS. Coculture of primary rat hepatocytes and nonparenchymal cells permits expression of insulin-like growth factor binding protein-3 in vitro. *Endocrinology.* May 1994;134(5):2044-2050.

36. Bader A, Knop E, Kern A, et al. 3-D coculture of hepatic sinusoidal cells with primary hepatocytes-design of an organotypical model. *Exp Cell Res.* Jul 10 1996;226(1):223-233.

37. Collins SD, Yuen G, Tu T, et al. In Vitro Models of the Liver: Disease Modeling, Drug Discovery and Clinical Applications. In: Tirnitz-Parker JEE, ed. *Hepatocellular Carcinoma*. Brisbane (AU): Codon Publications

38. Godoy P, Hewitt NJ, Albrecht U, et al. Recent advances in 2D and 3D in vitro systems using primary hepatocytes, alternative hepatocyte sources and non-parenchymal liver cells and their use in investigating mechanisms of hepatotoxicity, cell signaling and ADME. *Arch Toxicol.* Aug 2013;87(8):1315-1530.

39. Pettinato G, Lehoux S, Ramanathan R, et al. Generation of fully functional hepatocyte-like organoids from human induced pluripotent stem cells mixed with Endothelial Cells. *Scientific Reports.* 2019/06/20 2019;9(1):8920.

40. Alexander M, Loomis AK, Fairburn-Beech J, et al. Real-world data reveal a diagnostic gap in non-alcoholic fatty liver disease. *BMC Medicine.* 2018/08/13 2018;16(1):130.

41. Snyder JE, Hamid Q, Wang C, et al. Bioprinting cell-laden matrigel for radioprotection study of liver by pro-drug conversion in a dual-tissue microfluidic chip. *Biofabrication.* Sep 2011;3(3):034112.

42. Zhang S, Wang H. Current Progress in 3D Bioprinting of Tissue Analogs. *SLAS Technol.* Feb 2019;24(1):70-78.

43. Tomov ML, Theus A, Sarasani R, Chen H, Serpooshan V. 3D Bioprinting of Cardiovascular Tissue Constructs: Cardiac Bioinks. In: Serpooshan V, Wu SM, eds. *Cardiovascular Regenerative Medicine: Tissue Engineering and Clinical Applications*. Cham: Springer International Publishing; 2019:63-77.

44. Schmid J, Schwarz S, Meier-Staude R, et al. A Perfusion Bioreactor System for Cell Seeding and Oxygen-Controlled Cultivation of Three-Dimensional Cell Cultures. *Tissue Eng Part C Methods.* Oct 2018;24(10):585-595.

45. Knöspel F, Jacobs F, Freyer N, et al. In Vitro Model for Hepatotoxicity Studies Based on Primary Human Hepatocyte Cultivation in a Perfused 3D Bioreactor System. *Int J Mol Sci.* Apr 16 2016;17(4):584.

46. Serpooshan V, Mahmoudi M, Hu DA, Hu JB, Wu SM. Bioengineering cardiac constructs using 3D printing. *Journal of 3D Printing in Medicine.* 2017;1(2):123-139.

47. Cadena M, Ning L, King A, et al. 3D Bioprinting of Neural Tissues. *Advanced Healthcare Materials.*n/a(n/a):2001600.

48. Ryan AJ, Brougham CM, Garciarena CD, Kerrigan SW, O'Brien FJ. Towards 3D in vitro models for the study of cardiovascular tissues and disease. *Drug Discov Today.* Sep 2016;21(9):1437-1445.

49. Derakhshanfar S, Mbeleck R, Xu K, Zhang X, Zhong W, Xing M. 3D bioprinting for biomedical devices and tissue engineering: A review of recent trends and advances. Vol 3: Elsevier; 2018:144-156.

50. Zhang X, Zhang Y. Tissue Engineering Applications of Three-Dimensional Bioprinting. *Cell Biochem Biophys.* Jul 2015;72(3):777-782.

51. Lee S-J, Esworthy T, Stake S, et al. Advances in 3D Bioprinting for Neural Tissue Engineering. *Advanced Biosystems.* 2018;2(4):1700213.

52. Chung JHY, Naficy S, Yue Z, et al. Bio-ink properties and printability for extrusion printing living cells. *Biomaterials Science.* 2013;1(7):763-773.

53. O'Connell C, Ren J, Pope L, et al. Characterizing Bioinks for Extrusion Bioprinting: Printability and Rheology. *Methods Mol Biol.* 2020;2140:111-133.

54. Hospodiuk M, Dey M, Sosnoski D, Ozbolat IT. The bioink: A comprehensive review on bioprintable materials. *Biotechnol Adv.* Mar - Apr 2017;35(2):217-239.

55. Zhao Y, Li Y, Mao S, Sun W, Yao R. The influence of printing parameters on cell survival rate and printability in microextrusion-based 3D cell printing technology. *Biofabrication.* Nov 2 2015;7(4):045002.

56. Ji S, Guvendiren M. Recent Advances in Bioink Design for 3D Bioprinting of Tissues and Organs. *Frontiers in bioengineering and biotechnology.* 2017;5:23.

57. Shirahama H, Lee BH, Tan LP, Cho N-J. Precise Tuning of Facile One-Pot Gelatin Methacryloyl (GelMA) Synthesis. *Scientific Reports.* 2016/08/09 2016;6(1):31036.

58. Oliver WC, Pharr GM. Measurement of hardness and elastic modulus by instrumented indentation: Advances in understanding and refinements to methodology. *Journal of materials research.* 2004;19(1):3-20.

59. Oliver WC, Pharr GM. An improved technique for determining hardness and elastic modulus using load and displacement sensing indentation experiments. *Journal of materials research.* 1992;7(6):1564-1583.

60. Serpooshan V, Quinn TM, Muja N, Nazhat SN. Hydraulic permeability of multilayered collagen gel scaffolds under plastic compression-induced unidirectional fluid flow. *Acta Biomater.* Jan 2013;9(1):4673-4680.

61. Lee S, Serpooshan V, Tong X, et al. Contractile force generation by 3D hiPSC-derived cardiac tissues is enhanced by rapid establishment of cellular interconnection in matrix with muscle-mimicking stiffness. *Biomaterials.* Jul 2017;131:111-120.

62. Serpooshan V, Muja N, Marelli B, Nazhat SN. Fibroblast contractility and growth in plastic compressed collagen gel scaffolds with microstructures correlated with hydraulic permeability. *J Biomed Mater Res A.* Mar 15 2011;96(4):609-620.

63. Serpooshan V, Zhao M, Metzler SA, et al. The effect of bioengineered acellular collagen patch on cardiac remodeling and ventricular function post myocardial infarction. *Biomaterials.* Dec 2013;34(36):9048-9055.

64. Serpooshan V, Julien M, Nguyen O, et al. Reduced hydraulic permeability of three-dimensional collagen scaffolds attenuates gel contraction and promotes the growth and differentiation of mesenchymal stem cells. *Acta Biomater.* Oct 2010;6(10):3978-3987.

65. Du W, Wang X-T, Long Y, Liu D-W. Monitoring Changes in Hepatic Venous Velocities Flow after a Fluid Challenge Can Identify Shock Patients Who Lack Fluid Responsiveness. *Chin Med J (Engl).* 2017;130(10):1202-1210.

66. Eipel C, Abshagen K, Vollmar B. Regulation of hepatic blood flow: the hepatic arterial buffer response revisited. *World journal of gastroenterology.* 2010;16(48):6046-6057.

67. Ning L, Mehta R, Cao C, et al. Embedded 3D Bioprinting of Gelatin Methacryloyl-Based Constructs with Highly Tunable Structural Fidelity. *ACS Applied Materials & Interfaces.* 2020/10/07 2020;12(40):44563-44577.

68. Schwab A, Levato R, D'Este M, Piluso S, Eglin D, Malda J. Printability and Shape Fidelity of Bioinks in 3D Bioprinting. *Chemical Reviews.* 2020/10/14 2020;120(19):11028-11055.

69. Mazzocchi A, Soker S, Skardal A. 3D bioprinting for high-throughput screening: Drug screening, disease modeling, and precision medicine applications. *Applied Physics Reviews.* 2019;6(1):011302.

70. Peng W, Unutmaz D, Ozbolat IT. Bioprinting towards Physiologically Relevant Tissue Models for Pharmaceutics. *Trends in Biotechnology.* 2016;34(9):722-732.

71. Utama RH, Atapattu L, O'Mahony AP, et al. A 3D Bioprinter Specifically Designed for the High-Throughput Production of Matrix-Embedded Multicellular Spheroids. *iScience.* 2020/10/23/ 2020;23(10):101621.

72. Mouser VHM, Levato R, Mensinga A, Dhert WJA, Gawlitta D, Malda J. Bio-ink development for three-dimensional bioprinting of hetero-cellular cartilage constructs. *Connect Tissue Res.* Mar 2020;61(2):137-151.

73. Yue K, Trujillo-de Santiago G, Alvarez MM, Tamayol A, Annabi N, Khademhosseini A. Synthesis, properties, and biomedical applications of gelatin methacryloyl (GelMA) hydrogels. *Biomaterials.* Dec 2015;73:254-271.

74. Basara G, Yue X, Zorlutuna P. Dual Crosslinked Gelatin Methacryloyl Hydrogels for Photolithography and 3D Printing. *Gels.* Jul 3 2019;5(3).

75. Wang L, Zhu M, Cao L, et al. Liver Stiffness Measurement Can Reflect the Active Liver Necroinflammation in Population with Chronic Liver Disease: A Real-world Evidence Study. *J Clin Transl Hepatol.* 2019;7(4):313-321.

76. Roulot D, Czernichow S, Le Clésiau H, Costes JL, Vergnaud AC, Beaugrand M. Liver stiffness values in apparently healthy subjects: influence of gender and metabolic syndrome. *J Hepatol.* Apr 2008;48(4):606-613.

77. Noshadi I, Hong S, Sullivan KE, et al. In vitro and in vivo analysis of visible light crosslinkable gelatin methacryloyl (GelMA) hydrogels. *Biomaterials science.* 2017;5(10):2093-2105.

78. Wang Y, Ma M, Wang J, et al. Development of a Photo-Crosslinking, Biodegradable GelMA/PEGDA Hydrogel for Guided Bone Regeneration Materials. *Materials (Basel).* 2018;11(8):1345.

79. Aubin H, Nichol JW, Hutson CB, et al. Directed 3D cell alignment and elongation in microengineered hydrogels. *Biomaterials.* Sep 2010;31(27):6941-6951.

80. Ding H, Illsley NP, Chang RC. 3D Bioprinted GelMA Based Models for the Study of Trophoblast Cell Invasion. *Scientific Reports.* 2019/12/11 2019;9(1):18854.

81. Nichol JW, Koshy ST, Bae H, Hwang CM, Yamanlar S, Khademhosseini A. Cell-laden microengineered gelatin methacrylate hydrogels. *Biomaterials.* 2010;31(21):5536-5544.

82. Gilchrist AE, Lee S, Hu Y, Harley BAC. Soluble Signals and Remodeling in a Synthetic Gelatin-Based Hematopoietic Stem Cell Niche. *Advanced Healthcare Materials.* 2019;8(20):1900751.

83. Eitan Y, Sarig U, Dahan N, Machluf M. Acellular cardiac extracellular matrix as a scaffold for tissue engineering: in vitro cell support, remodeling, and biocompatibility. *Tissue Eng Part C Methods.* Aug 2010;16(4):671-683.

84. Wang K, Lin B. Pathophysiological Significance of Hepatic Apoptosis. *ISRN Hepatology.* 2012/12/30 2013;2013:740149.

85. Vinken M, Maes M, Oliveira AG, et al. Primary hepatocytes and their cultures in liver apoptosis research. *Archives of toxicology.* 2014;88(2):199-212.

86. Rui L. Energy metabolism in the liver. *Compr Physiol.* 2014;4(1):177-197.

87. Nagarajan SR, Paul-Heng M, Krycer JR, Fazakerley DJ, Sharland AF, Hoy AJ. Lipid and glucose metabolism in hepatocyte cell lines and primary mouse hepatocytes: a comprehensive resource for in vitro studies of hepatic metabolism. *American Journal of Physiology-Endocrinology and Metabolism.* 2019;316(4):E578-E589.

88. Lauschke VM, Shafagh RZ, Hendriks DFG, Ingelman-Sundberg M. 3D Primary Hepatocyte Culture Systems for Analyses of Liver Diseases, Drug Metabolism, and Toxicity: Emerging Culture Paradigms and Applications. *Biotechnology Journal.* 2019;14(7):1800347.

89. Cassim S, Raymond V-A, Lapierre P, Bilodeau M. From in vivo to in vitro: Major metabolic alterations take place in hepatocytes during and following isolation. *PLOS ONE.* 2017;12(12):e0190366.

90. Huang T, Jones CG, Chung JH, Chen C. Microfibrous Extracellular Matrix Changes the Liver Hepatocyte Energy Metabolism via Integrins. *ACS Biomaterials Science & Engineering.* 2020/10/12 2020;6(10):5849-5856.

91. Stiehler M, Bünger C, Baatrup A, Lind M, Kassem M, Mygind T. Effect of dynamic 3-D culture on proliferation, distribution, and osteogenic differentiation of human mesenchymal stem cells. *J Biomed Mater Res A.* Apr 2009;89(1):96-107.

92. Massai D, Isu G, Madeddu D, et al. A Versatile Bioreactor for Dynamic Suspension Cell Culture. Application to the Culture of Cancer Cell Spheroids. *PLOS ONE.* 2016;11(5):e0154610.

93. Tsai HH, Yang KC, Wu MH, Chen JC, Tseng CL. The Effects of Different Dynamic Culture Systems on Cell Proliferation and Osteogenic Differentiation in Human Mesenchymal Stem Cells. *Int J Mol Sci.* Aug 17 2019;20(16).

94. Wang G, Zheng Y, Wang Y, et al. Co-culture system of hepatocytes and endothelial cells: two in vitro approaches for enhancing liver-specific functions of hepatocytes. *Cytotechnology.* 2018;70(4):1279-1290.

95. Underhill GH, Khetani SR. Emerging trends in modeling human liver disease in vitro. *APL Bioeng.* Dec 2019;3(4):040902.

96. Cetnar AD, Tomov ML, Ning L, et al. Patient-Specific 3D Bioprinted Models of Developing Human Heart. *Adv Healthc Mater.* Dec 4 2020:e2001169.

97. Zhao D, Xue C, Li Q, et al. Substrate stiffness regulated migration and angiogenesis potential of A549 cells and HUVECs. *J Cell Physiol.* Apr 2018;233(4):3407-3417.

98. La W-G, Yang HS. Synergistic effects of extracellular matrix rigidity and immobilized vascular endothelial growth factor on vascular tube formation and cell morphology of human umbilical vein endothelial cells. *Tissue Engineering and Regenerative Medicine.* 2015/02/01 2015;12(1):20-27.

99. DiVito KA, Daniele MA, Roberts SA, Ligler FS, Adams AA. Microfabricated blood vessels undergo neoangiogenesis. *Biomaterials.* Sep 2017;138:142-152.

100. Lee J-H, Parthiban P, Jin G-Z, Knowles JC, Kim H-W. Materials roles for promoting angiogenesis in tissue regeneration. *Progress in Materials Science.* 2021/04/01/ 2021;117:100732.

101. Vailhé B, Vittet D, Feige J-J. In Vitro Models of Vasculogenesis and Angiogenesis. *Laboratory Investigation.* 2001/04/01 2001;81(4):439-452.

102. Scheinfeld MH, Bilali A, Koenigsberg M. Understanding the Spectral Doppler Waveform of the Hepatic Veins in Health and Disease. *RadioGraphics.* 2009;29(7):2081-2098.